



OPEN ACCESS

EDITED BY

Yongsheng He,
China University of Geosciences, China

REVIEWED BY

Wang Fangyue,
Hefei University of Technology, China
Majid Ghaderi,
Tarbiat Modares University, Iran

*CORRESPONDENCE

Qingdong Zeng,
✉ zengqingdong@mail.iggcas.ac.cn

RECEIVED 12 December 2023

ACCEPTED 17 January 2024

PUBLISHED 21 February 2024

CITATION

Zhang Z, Zeng Q, Fan H-R, Bai R, Wu J, Li X, Zhang Y and Huang L (2024), Characterization of deep ore-forming fluid in the Zhaoxian gold deposit within the Jiaodong gold province: insights from quartz vein fluid inclusion, *in-situ* trace element analysis, and S isotopic composition in pyrite. *Front. Earth Sci.* 12:1354261. doi: 10.3389/feart.2024.1354261

COPYRIGHT

© 2024 Zhang, Zeng, Fan, Bai, Wu, Li, Zhang and Huang. This is an open-access article distributed under the terms of the [Creative Commons Attribution License \(CC BY\)](https://creativecommons.org/licenses/by/4.0/). The use, distribution or reproduction in other forums is permitted, provided the original author(s) and the copyright owner(s) are credited and that the original publication in this journal is cited, in accordance with accepted academic practice. No use, distribution or reproduction is permitted which does not comply with these terms.

Characterization of deep ore-forming fluid in the Zhaoxian gold deposit within the Jiaodong gold province: insights from quartz vein fluid inclusion, *in-situ* trace element analysis, and S isotopic composition in pyrite

Zheming Zhang^{1,2,3}, Qingdong Zeng^{3,4*}, Hong-Rui Fan^{3,4}, Rui Bai⁵, Jinjian Wu^{1,3,4}, Xinghui Li³, Yongwen Zhang⁶ and Liangliang Huang³

¹Shandong Engineering Research Center of Application and Development of Big Data for Deep Gold Exploration, Weihai, China, ²Sinosteel Overseas Resources Limited, Beijing, China, ³Key Laboratory of Mineral Resources, Institute of Geology and Geophysics, Chinese Academy of Sciences, Beijing, China, ⁴College of Earth and Planetary Sciences, University of Chinese Academy of Sciences, Beijing, China, ⁵Shandong Gold Geology and Mineral Exploration Co., Ltd., Laizhou, Shandong, China, ⁶Jiangxi Mineral Resources Guarantee and Service Center, Nanchang, China

The Jiaodong gold province, situated in the southeastern margin of the North China Craton, is globally renowned for its substantial gold reserves exceeding 5,000 tonnes. The Zhaoxian gold deposit is part of the significant Jiaojia gold belt within the Jiaodong gold province. Fieldwork has identified four distinct stages of ore formation in this study: an early barren quartz vein stage (Stage 1) containing fine-grained pyrite; a gold-bearing stage (Stage 2) consisting of quartz, pyrite, and native gold; a polymetallic sulfide-rich stage (Stage 3) comprising quartz, polymetallic sulfides, and native gold; and a late-stage (Stage 4) primarily composed of quartz and calcite with minimal pyrite content. We conducted fluid inclusion analysis using microthermometry and Raman spectroscopy techniques to examine the fluid characteristics. *In-situ* analysis of trace elements in pyrite was performed to investigate the fluid composition and evolution. Additionally, we determined the sulfur isotope composition in pyrite to analyze the source of sulfur. Our findings indicate that the ore-forming fluid in the Zhaoxian gold deposit belongs to a medium-to-low-salinity H₂O-NaCl-CO₂-CH₄ system. Fluctuations in Au and As concentrations observed along with oscillating zones and sulfide inclusions during Stage 2 suggest potential fluid boiling processes occurring during mineralization. High concentrations of Ag, Cu, Zn, Cd, In, Pb, and Bi without oscillating zones during Stage 3 imply precipitation of polymetallic sulfides under stable fluid conditions. The $\delta^{34}\text{S}$ values observed in the Zhaoxian gold deposit are slightly higher than those found in granitoids from other areas within Jiaodong but similar to those seen

in other deposits within the Jiaojia gold belt region. In conclusion, magmatic-hydrothermal ore-forming fluids were involved along with significant fluid-rock interaction during metallogenic processes of the Zhaoxian gold deposit.

KEYWORDS

Zhaoxian gold deposit, the southeast margin of the North China Craton, *in-situ* trace element analyzing, *in-situ* sulfide isotope, ore-forming process

1 Introduction

The Jiaodong gold province is a globally significant gold district with reserves exceeding 5,000 tonnes (Fan et al., 2016; Deng et al., 2020). Understanding the characteristics, sources, enrichment, and metallogenic mechanisms of these gold deposits, as well as developing a comprehensive genetic model for their formation, are key focal points in ore deposit research. However, ongoing debate persists regarding the genetic mechanism accountable for the formation of these gold deposits, encompassing divergent viewpoints such as non-orogenic (Zhai et al., 2004), orogenic (Goldfarb and Groves, 2015; Groves et al., 2020), Jiaodong-type (Li et al., 2015; Deng et al., 2020), and decratonic models (Zhu et al., 2015).

The Jiaojia gold belt controls significant gold deposits including Jiaojia, Xincheng, Sizhuang, Shaling, Qianchen-Shangyangjia, and Zhaoxian (Fan et al., 2007; Wen et al., 2016; Cai et al., 2018; Wu et al., 2022). Although extensive exploratory efforts have been made in this gold belt, there is a need for comprehensive investigations into various aspects such as the subterranean geological characteristics of orebodies beyond a depth of 1 km and more detailed metallogenic mechanisms. The Zhaoxian gold deposit within the Jiaojia gold belt is particularly interesting due to the drill cores accessible at depths ranging from 2,200 m to 1,500 m below sea level—significantly exceeding the typical depth of most gold deposits (<800 m) in the Jiaojia-Xincheng gold deposit belt. This presents an exceptional opportunity to gather comprehensive information on deep mineralization and gain insights into the deep-forming mechanism of the Jiaojia gold belt. Previous studies in the Zhaoxian gold deposit have involved micro region analysis, *in-situ* pyrite analysis (Li et al., 2021; Xu et al., 2022), a three-dimensional metallogenic prospecting model (Li et al., 2022), as well as investigations on fluid inclusion at depths ranging from 2,146 to 2,038 m below sea level (Li et al., 2023). However, further investigations are necessary to examine the properties of ore-forming fluids and elucidate the sources of sulfur. Moreover, comprehensive and detailed explanations are required for the diverse assay data.

In this study, we collected deep drill cores (1,731 m to 1,372 m below sea level) from the Zhaoxian gold deposit for analysis. After conducting comprehensive fieldwork and meticulous petrological studies under a high-powered microscope, we judiciously handpicked fresh and representative samples for subsequent laboratory analysis. We measured the homogeneous temperatures of fluid inclusions at each stage and determined their salinities based on freezing points (biphase aqueous inclusion), as well as the final melting temperature of CO₂-H₂O clathrate (CO₂-rich inclusion). Additionally, laser-Raman spectroscopy was employed to analyze the volatile compositions of fluid inclusions in each stage. The

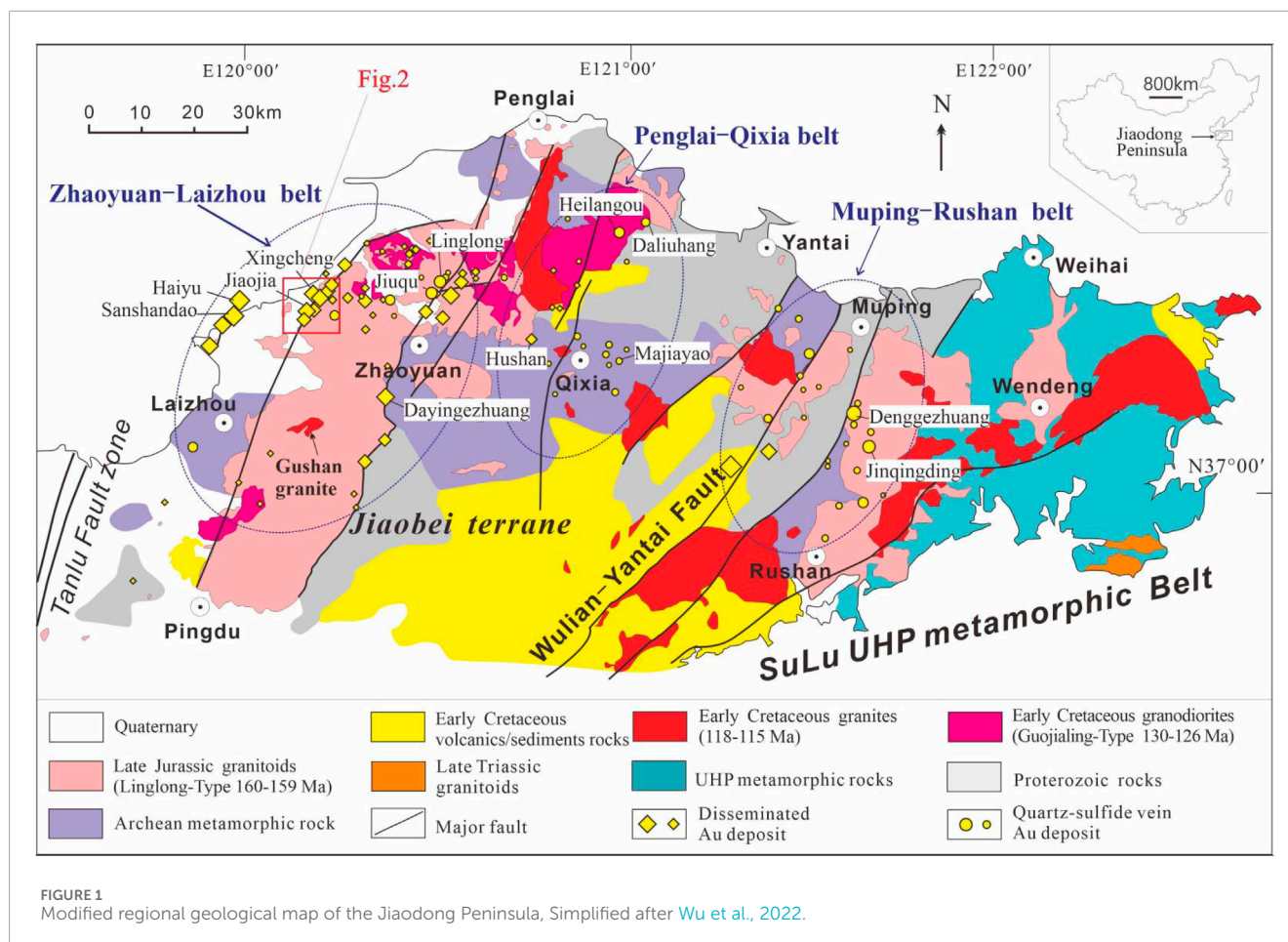
trace element content and composition in pyrite were quantified to elucidate the evolution of ore-forming fluid. In order to gain insights into the sulfur source in each stage, we investigated the *in-situ* sulfur isotope composition in pyrite within the Zhaoxian gold deposit. Furthermore, we made a detailed discussion of the mineralization process. From the above work, we contend that the Zhaoxian gold deposit underwent a multiple mineralization process and represents a prototypical magmatic-hydrothermal deposit within the Jiaodong region.

2 Geological setting

The Jiaodong gold province is located in the southeastern margin of the North China Craton (NCC), specifically within the eastern segment of the Tanlu fault zone based on its tectonic distribution (Figure 1).

The Jiaodong Peninsula can be geologically classified into two distinct regions, namely, the Jiaobei terrane (western part) and the Sulu ultra-high pressure (UHP) metamorphic belt (eastern part), which are separated by the Wulian-Yantai fault belt (Zhou et al., 2008). The Jiaobei terrane encompasses both the southern Jiaolai Basin and the northern Jiaobei uplift. Within the Jiaolai Basin, there exist volcanic rocks from the Cretaceous Qingshan Formation (110Ma–108Ma) as well as sedimentary rocks from the Laiyang Formation (Qiu et al., 2001; Liu et al., 2009; Xie et al., 2012). The exposed rocks in the study area are predominantly Precambrian metamorphic basement rocks, including amphibolite to granulite facies metamorphic rocks such as the Neoproterozoic Jiaodong Group consisting of volcanic-sedimentary rocks and tonalite-trondhjemite-granodiorite gneisses, Proterozoic Fenzishan and Jingshan Group comprising meta-volcanic and metasedimentary rocks, along with Penglai Group composed of meta-sedimentary rocks (Zhou and Lü, 2000; Jahn et al., 2008; Dong et al., 2010; Zhai and Santosh, 2013; Zou et al., 2017).

Mesozoic granites have extensively intruded ultra-high pressure (UHP) metamorphic rocks in the Jiaodong Peninsula (Figure 1). These granites consist of late Jurassic granites (170Ma–150Ma), which formed through remelting of the thickened lower crust, such as Linglong granite and Luanjiahe granite (Jiang et al., 2012; Yang et al., 2012; Ma et al., 2013). Additionally, there are early Cretaceous granites (132Ma–126Ma) that originated from a mixture of lower crustal melt and mantle components, including Guojialing, Sanshandao, Congjia, Beijie, and Shangzhuang (Yang et al., 2012; 2014). The porphyritic syenogranite and monzogranite (120Ma–110Ma), primarily composed of Aishan and Gushan granitoids (Goss et al., 2010; Li et al., 2012; 2019), as well as mafic dikes (121Ma–87Ma, Li et al., 2019), were formed



during late early Cretaceous through the process of ancient crustal material melting and upwelling of lithospheric mantle material, respectively (Ma et al., 2014).

The distribution of ore occurrences in the Jiaodong Peninsula is primarily controlled by three gold belts, namely, the Zhaoyuan-Laizhou, Penglai-Qixia, and Muping-Rushan gold belts from west to east. Most of the gold deposits are hosted in the Linglong and Guojialing granitoids or their contacts with basement metamorphic rocks. These deposits are distributed along a series of NE–NNE-trending faults, including Sanshandao, Jiaoqia, Zhaoyuan-Pingdu, Qixia, and Muping faults (Figure 1). The Zhaoxian gold deposit is situated within the Zhaoyuan-Laizhou gold belt, with its ore-controlling structure represented by the Jiaoqia-Xincheng fault.

In the Jiaodong gold province, researchers have categorized gold deposits into two primary styles based on their mineralized form: disseminated style and auriferous quartz vein style (Zhou and Lü, 2000; Fan et al., 2007; Goldfarb and Santosh, 2014; Wen et al., 2015). Disseminated-style deposits display extensive dissemination of gold mineralization occurring along regional faults, accompanied by widespread alteration halos. The Zhaoyuan-Laizhou gold belt is the primary host for large disseminated-style deposits, accounting for approximately 90% of the total gold reserves in the Jiaodong Peninsula (Song, 2015; Fan et al., 2016; Yang et al., 2016). In contrast, auriferous quartz vein-style deposits are characterized by numerous subsidiary faults of lower orders hosting gold-bearing

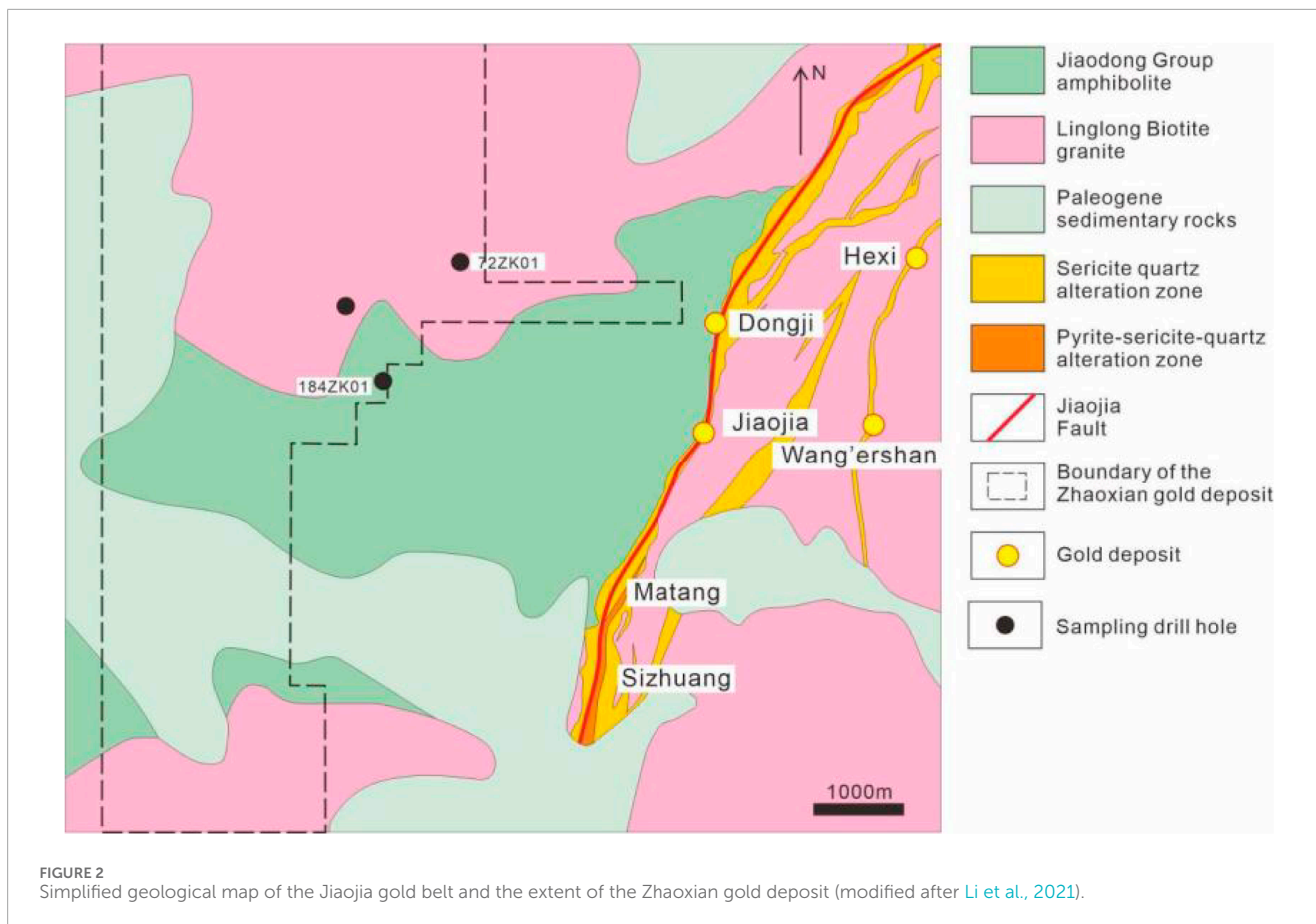
quartz veins. Medium to large-scale auriferous quartz vein style-gold deposits dominate within the Penglai-Qixia belt, with the exception of the Hushan deposit which exhibits disseminated-style mineralization (Feng et al., 2018; Yang et al., 2018).

3 Ore deposit geology

3.1 Basic geology

The Zhaoxian gold deposit is located within the central part of the Jiaoqia fault zone, where it is exposed to Paleoproterozoic granulite, marble, and schist of the Jingshan Group, as well as pelitic arkose and clay sandstone (Wutu Group) of the Cenozoic Zhubidian Formation (Zhu et al., 2018; Figure 2).

The Jiaoqia fault zone is a large fault zone within the Jiaodong gold province, comprising more than 10 parallel northwest-trending faults with an approximate width of 6 km. The fault zone has a slightly undulating shape and a width ranging from 500 m to 1,000 m. The strikes of the faults are nearly northwest, and their dips average around 40°. Both ends of the fault zone are covered by Quaternary strata along its strike. The Jiaoqia fault, located within the Jiaoqia fault zone, plays a significant role as the main controlling fault governing mineral deposition. The fault has a considerable width ranging from 160 m to 500 m and has a slightly undulating shape.



The fault exhibits varying trends between 0° and 30° in a west-northwest direction with a gentle dip angle. The northern segment of the fault has an average dip angle of 19° , ranging from 10° to 26° , while the southern segment exhibits an average dip angle of 27° , ranging from 12° to 40° . The central region of the Jiaojia fault exhibits a continuous and stable main fracture plane, characterized by fault gouge with thicknesses ranging from 1 cm to 30 cm. The tectonic rocks in the Jiaojia fault zone can be classified into three lithologic zones based on their degree of fragmentation. The internal zone consists of mylonites and cataclastic rocks with an approximate average thickness of 20 m. The middle zone primarily comprises granitic cataclastic and metabro cataclastic rocks, with an average thickness of around 50 m. The outer zone encompasses sericite granite along with sericite metabro belts, which have an average thickness of approximately 200 m. While most boundaries between these lithologic zones demonstrate a gradual transition, certain boundaries exhibit more distinct characteristics. Within the mining area, various magmatic rocks can be found including metamorphic gabbros (Figure 2), Qixia gneisses, biotite schists; early Yanshanian Linglong medium-grained monzonitic granites displaying weak gneissosity; late Yanshanian Guojialing porphyritic granodiorites; in addition to several younger dikes.

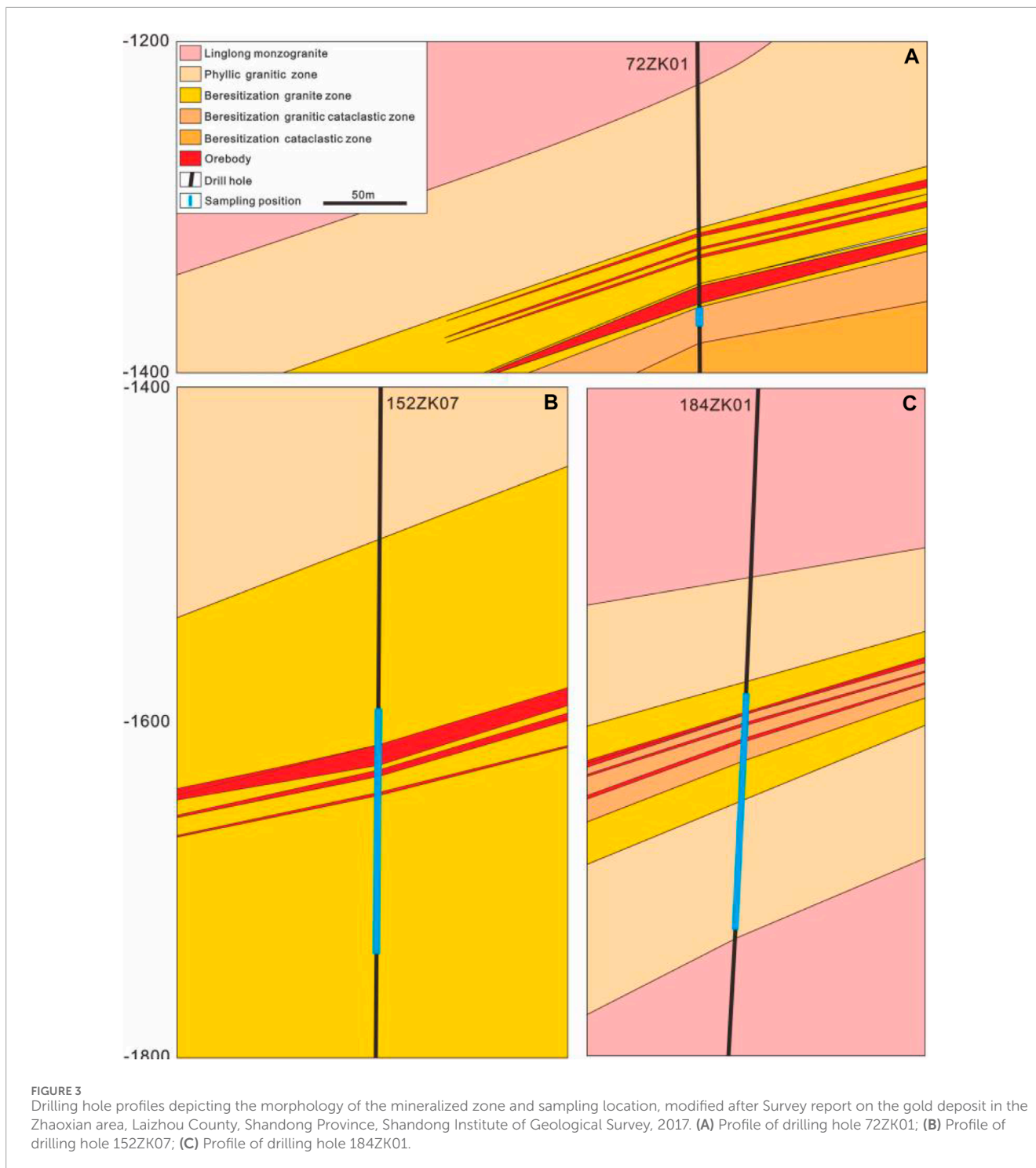
3.2 Orebodies

According to estimates, the potential gold resource in the Zhaoxian gold deposit exceeds 100 tonnes (Survey report on the gold

deposit in the Zhaoxian area, Laizhou County, Shandong Province, Shandong Institute of Geological Survey, 2017). The Zhaoxian gold deposit likely consists of fissure-altered ore, containing a total of 27 orebodies located within faults and clastic zones (Figure 3). These ore bodies range in elevation from 2,144 m to 1,260 m below sea level and are aligned along fault lines trending between 236° and 345° with a dip angle ranging from 11° to 27° . The thicknesses of the orebodies range from 0.95 m to 13.83 m, exhibiting gold grades varying between 0.10 g/t and 18.40 g/t.

3.3 Hydrothermal stages and ore mineralogy

We conducted comprehensive mineralogical investigations, including both macroscopic and microscopic observations. By examining the mineral characteristics under an optical microscope, we can distinguish different mineral phases. In cases where identifying certain minerals becomes difficult, we can use a scanning electron microscope-backscattered electron (SEM-BSE). For example, native gold appears as a brighter and more vibrant golden yellow color compared to chalcopyrite; when the mineral grains are indistinguishable at small scales, SEM analysis helps in identifying the minerals: native gold appears as a brilliant white shade in SEM images while chalcopyrite manifests as a dark gray color. The metallogenic process can be categorized into four stages based on the crosscut relationship and mineral coexistence



association. Figures 4A–D display the representative ores in each stage, while Figures 4E–G display the crosscuts between these stages.

Stage 1 (early stage, barren coarse-grained quartz vein with fine-grained pyrite, Figure 4A) primarily consists of milky quartz veins ranging from 1 cm to 4 cm in width. The quartz grains show both ductile and brittle deformation, and there is a small amount of fine-grained pyrite (Py1, Figures 5A, B, 7A, 8A), with K-feldspar also present (Figure 4A). Only a little fine-grained pyrite found in this stage, however, other sulfide and native gold did not found.

Stage 2 (gold stage, composed of smoky fine-grained quartz, coarse-grained pyrite, allotriomorphic chalcopyrite, and native gold, Figures 4B, E) is characterized by the abundant presence of pyrite (Py2) among the ore minerals. The pyrite crystals in this stage have a relatively high degree of crystallinity and generally possess coarse grains and of idiomorphic-hypidiomorphic aggregates with oscillating zones (Figures 5C, D, 6B, 7B), which is an identifying mark of this stage. Native gold grains can be observed within the pyrite grains or within fissures in quartz or pyrite grains (Figures 5C, 6B, C, 7B). The fine-grained smoky appearance of

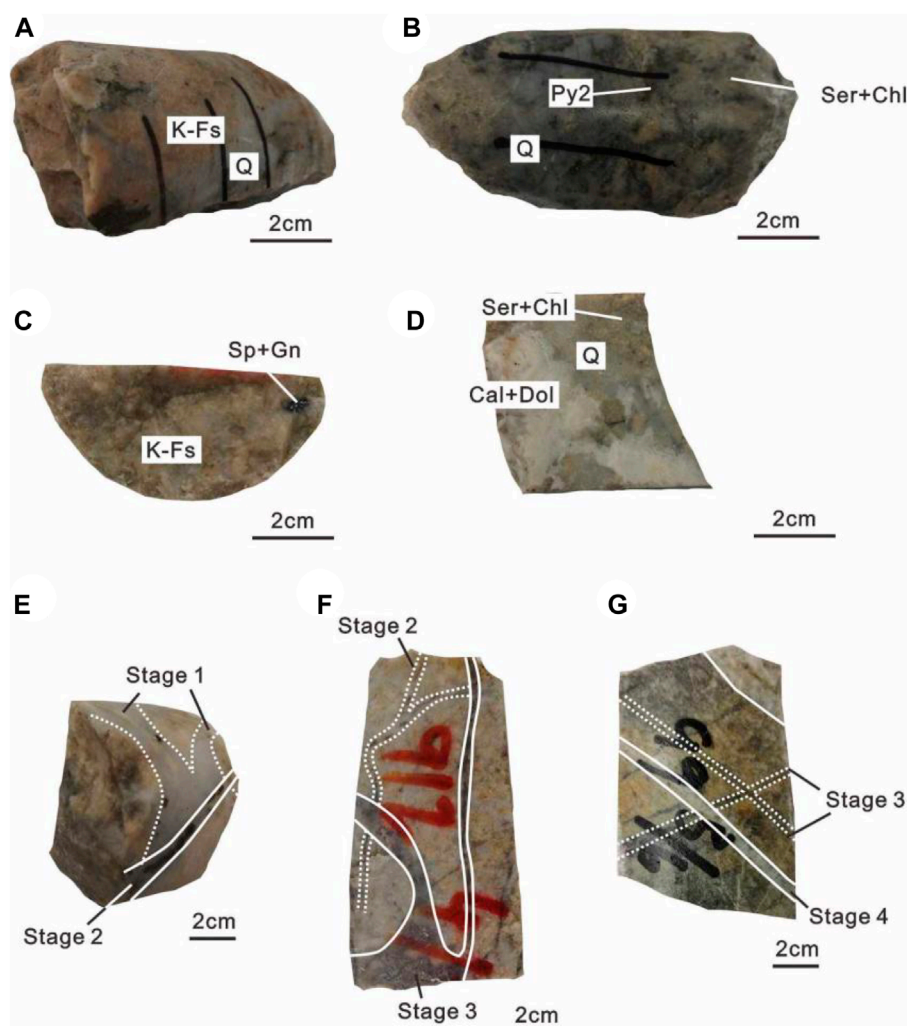


FIGURE 4

Photographs of hand specimens illustrating the geological features observed in the Zhaoxian gold deposit. (A) Stage 1 ore exhibits milky quartz veins hosted by potassic-altered rocks; (B) Stage 2 ore displays auriferous smoky quartz veins with sericitization and chloritization occurring within the host rock; (C) Stage 3 ore displays Pb-Zn mineralization occurring in a smoky quartz vein; (D) Stage 4 ore presents transparent off-white quartz-carbonate veins exhibiting sericitization and chloritization within the host rock; (E) Stage 2 gold stage quartz-pyrite-native gold veins crosscut Stage 1 early stage barren quartz veins; (F) Stage 3 polymetallic veins crosscut Stage 2 gold stage quartz-pyrite-native gold veins; (G) Stage 4 late stage quartz-calcite ± pyrite veins crosscut Stage 3 polymetallic veins. Abbreviations: Cal = calcite, Chl = chlorite, Dol = dolomite, Gn = galena, K-Fs = K-feldspar, Py = pyrite, Q = quartz, Ser = sericite, Sp = sphalerite.

the quartz veins signifies their significance as primary conduits for gold mineralization (Abdelkarim et al., 2022; Khedr et al., 2013; 2023; Figure 4B). Chalcopyrite is also common in this stage, which filled in the fractures of quartz and pyrite (Figures 5D, 7B). Stage 2 veins often crosscut Stage 1 veins, which shows that Stage 2 veins formed latter than preexisting Stage 1 veins (Figure 4E). The gold mineralization in this stage exhibits the most prominent manifestation compared to all other stages.

Stage 3 (polymetallic stage, composed of fine-grained smoky quartz, coarse-grained pyrite, sphalerite, galena, chalcopyrite, and native gold, Figures 4C, F) predominantly exhibits a fine and idiomorphic-hypidiomorphic morphology, with pyrite serving as the primary sulfide mineral (Figures 5E, F, 6D, 7C) that frequently undergoes replacement by chalcopyrite, galena, and sphalerite

(Figures 5F, 6E, 7C), sulfides mainly filled in the fissures of quartz (Figure 5F–H, 6E). In this stage, the proportion of sulfide is larger than that of previous stages. Stage 3 veins often crosscut Stage 2 veins, which shows that Stage 3 veins formed latter than preexisting Stage 2 veins (Figure 4F).

Stage 4 (late stage, composed of transparent quartz, calcite with a little pyrite, Figures 4D, G) contains an abundance of off-white quartz alongside transparent quartz-calcite veins containing some hypidiomorphic pyrite (Figures 5I, 6F, 7D). Stage 4 veins often crosscut Stage 3 veins, which shows that Stage 4 veins formed latter than preexisting Stage 3 veins (Figure 4G).

The major mineral paragenetic sequence is illustrated in Figure 8.

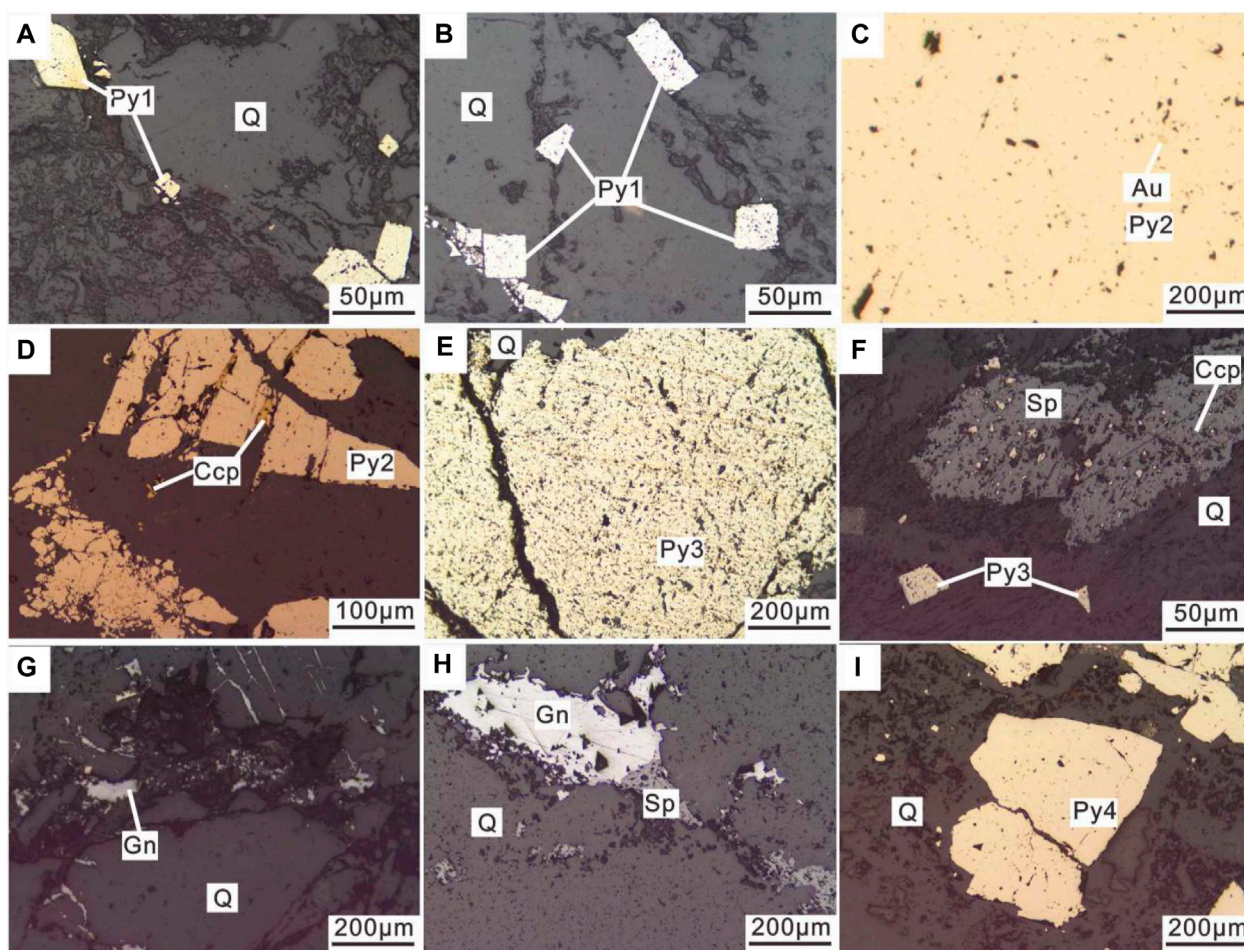


FIGURE 5

Micrographs illustrating paragenetic associations in the Zhaoxian gold deposit. (A, B) Fine-grained pyrite within Stage 1 vein; (C) Native gold grain enclosed by pyrite from Stage 2; (D) Chalcopyrite coexisting with and crosscutting pyrite in Stage 2; (E) Pyrite observed in Stage 3; (F) Sphalerite-altered pyrite in Stage 3; (G, H) Galena and sphalerite filling fissures within the quartz vein during Stage 3; (I) Pyrite present in Stage 4. Abbreviations: Au = native gold, Ccp = chalcopyrite, Gn = galena, Py = pyrite, Q = quartz, Sp = sphalerite.

3.4 Wall-rock alteration

The wall rock alteration within the Zhaoxian gold deposit is widespread and predominantly characterized by potassic alteration, beresitization, chloritization zone, and carbonatization alteration. The alteration phenomenon exhibits evident symmetry (Figure 3), with the ore body as the focal point and a gradual decrease in alteration intensity. Most of the ore bodies belong to altered-rock type. Each prospecting profile often encompasses multiple zones of alteration, including beresitization cataclastic zone, beresitization granitic cataclastic zone, beresitization granite zone, and phyllic granite zone (reference to Survey report on the gold deposit in the Zhaoxian area, Laizhou County, Shandong Province, Shandong Institute of Geological Survey, 2017). Potassic alteration is a high-temperature alteration, often found in the wall rock alongside high-temperature veins (Figure 9A). Beresitization refers to a moderate to high-temperature wall-rock alteration characterized by the presence of pyrite, quartz, sericite, etc. (Figure 9B). It primarily occurs in medium-acid igneous rocks and metamorphic rocks under the influence of hydrothermal

fluids at moderate to low temperatures. Beresitization may have a strong relationship with gold mineralization (Figure 9B). During this process, feldspar undergoes decomposition into sericite and quartz, while dark minerals are replaced by pyrite (Khedr et al., 2013; 2023; Abdelkarim et al., 2022). Chloritization (Figure 9C) appears to have a lower temperature than that of beresitization, and it can be found near the polymetallic stage. In this process, dark minerals like biotite and amphibolite are altered by chlorite. Carbonatization (Figure 9D) occurs at low temperatures and can be found near the late stage. Comparing with the wall-rock alteration works in previous researches (Li et al., 2022; Xu et al., 2022), we found that the alteration type in the Zhaoxian gold deposit is similar at different depths.

4 Sampling and analytical techniques

For this study, we meticulously collected 53 samples from three representative drill cores, namely, 72ZK01 (Figure 3A), 152ZK07 (Figure 3B), and 184ZK01 (Figure 3C), retrieved

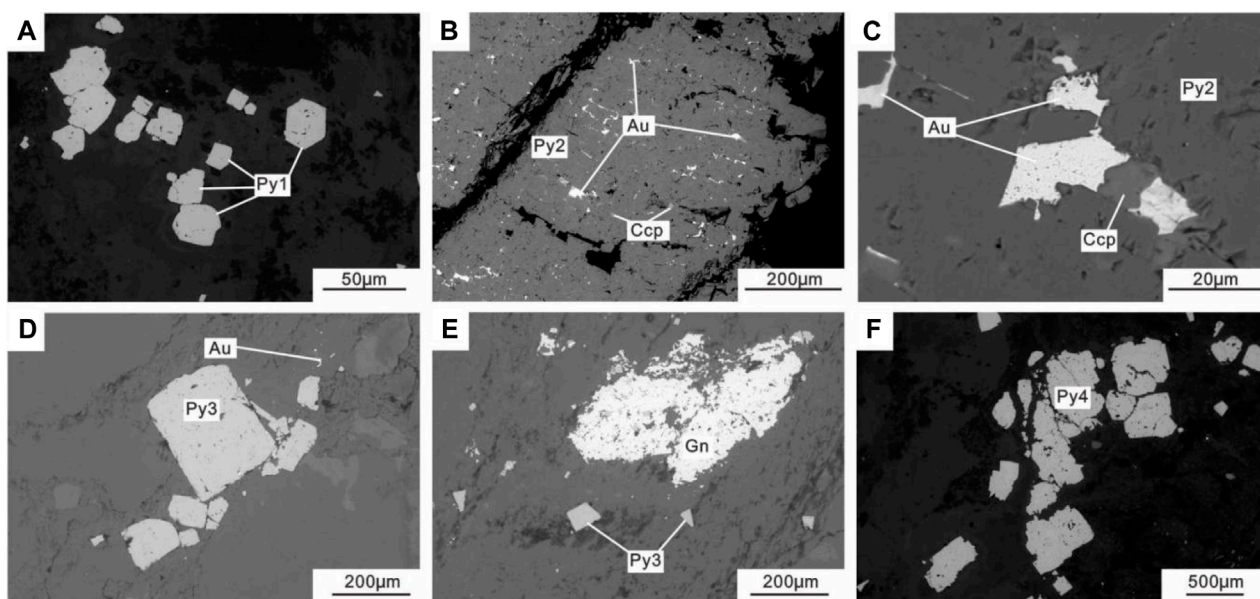


FIGURE 6
BSE images displaying sulfide minerals in different stages. (A) Idiomorphic-hypidiomorphic fine-grained pyrite in Stage 1 (Py1); (B,C) Native gold grains and branches within pyrite (Py2) fissures in Stage 2; (D) Homogeneous composition of Pyrite in Stage 3 (Py3); (E) Galena and pyrite (Py3) within polymetallic-quartz vein in Stage 3; (F) Pyrite within quartz-carbonate±pyrite in Stage 4. Abbreviations: Au = native gold, Ccp = chalcopyrite, Gn = galena, Py = pyrite.

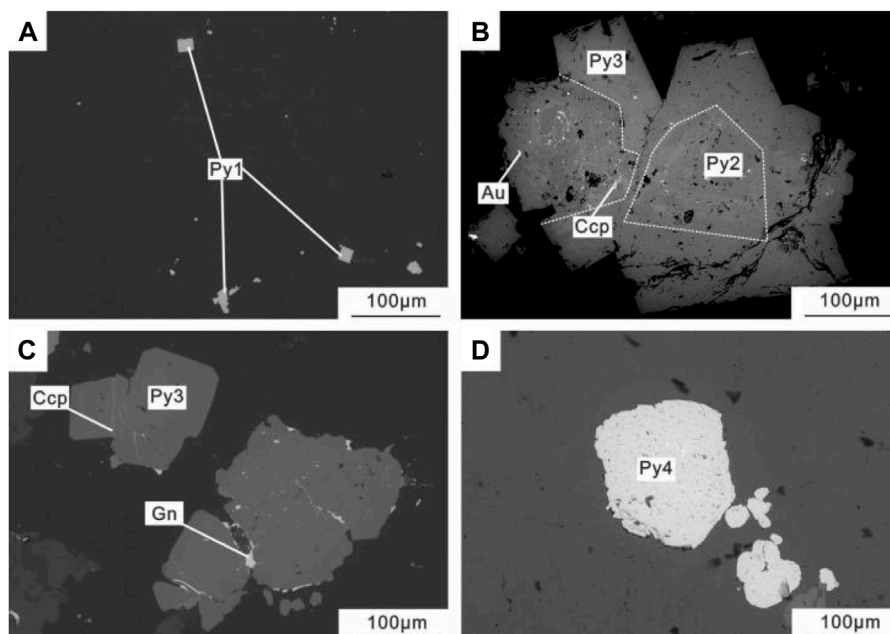
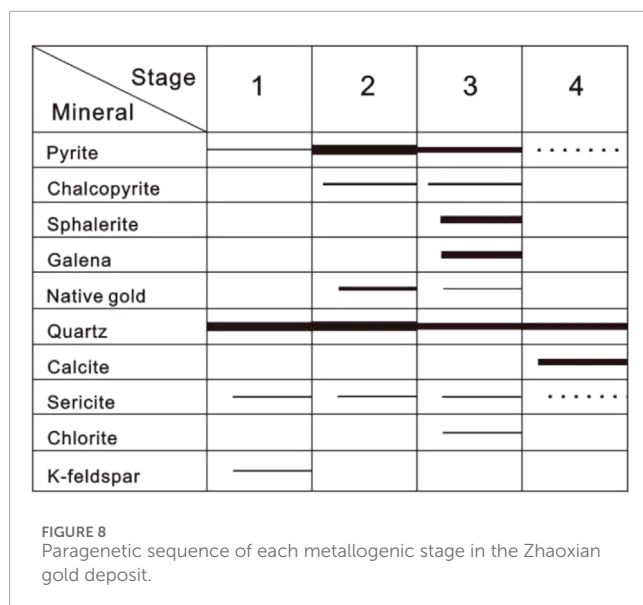


FIGURE 7
BSE images of pyrite in different stages. (A) Idiomorphic-hypidiomorphic fine-grained pyrite in Stage 1 (Py1) has a homogeneous composition. (B) Small native gold, chalcopyrite and galena inclusions can be found in the pyrite in Stage 2 (Py2) with oscillating zonation, the pyrite of Stage 3 (Py3) is almost homogeneous in composition, and replaced Py2. (C) Py3 is almost homogeneous in composition, with large mineral inclusions irregularly distributed, few zonations can be found in this type of pyrite. (D) Few sulfide inclusions can be found in the pyrite in Stage 4 (Py4), which has a homogeneous composition. Abbreviations: Au = native gold, Ccp = chalcopyrite, Gn = galena, Py = pyrite.



at depths ranging from 1,731 m to 1,372 m below sea level. Distinct samples were collected for fluid inclusion and pyrite *in-situ* analysis, encompassing sulfur isotopes and trace elements. We scrupulously differentiated various veins from different stages to facilitate subsequent experimental differentiation.

4.1 Mineral microanalysis

In order to conduct a detailed analysis of the minerals, representative samples from the Zhaoxian gold deposit were selected for mineralogy and petrology analyses. The Phenom XL scanning electron microscope (SEM) was utilized for precise mineral identification at the Institute of Geology and Geophysics, Chinese Academy of Sciences (IGGCAS), Beijing, China. Equipped with an energy-dispersive X-ray spectrometer (EDS), the SEM captured backscattered electron (BSE) images using an accelerating voltage of 15 kV and beam current of 3 nA or 4 nA through its user interface. Each BSE image was acquired over a duration of 1 min, while semi-quantitative point analyses were performed for 30 s.

4.2 Analysis of fluid inclusion

The quartz veins thin sections, with a thickness of approximately 0.2mm, were meticulously polished for the purpose of studying fluid inclusion and used for mineralogical and fluid inclusion analyses. The studies on inclusion were conducted using microthermometry and Raman spectroscopy techniques. All samples from four different stages of quartz veins contained suitable fluid inclusion assemblages, including primary, secondary, and pseudo-secondary fluid inclusions with identified fluid phases according to (Lu et al., 2004). Microthermometric measurements were conducted at IGGCAS using a THMS 600 programmable heating/freezing stage equipped with a Carl Zeiss Axioskop 40 and Nikon transmission/reflection optical microscope+camera system

that allowed direct observation of changes in the phase states during heating or freezing and measured the final melting temperature of solid CO₂ phase (T_{m,CO_2}), the final melting temperature of CO₂-H₂O clathrate ($T_{m,Cl}$), the homogenization temperature of CO₂ phases in the inclusion (T_{h,CO_2}) of CO₂-rich inclusion; the final melting temperature of ice (T_{m-ice}) of biphasic aqueous inclusion; and the homogenization temperature (T_{h-tot}) of CO₂-rich inclusion and biphasic aqueous inclusion. The accuracy of the freezing/heating measurements was estimated to be $\pm 0.1^\circ\text{C}$ below 30°C , $\pm 1^\circ\text{C}$ between 31°C and 300°C , and $\pm 2^\circ\text{C}$ above 300°C . Salinities of H₂O-NaCl fluids were calculated based on the measured T_{m-ice} using the method described in (Bodnar, 1993), while salinities of H₂O-CO₂ fluids were calculated based on the measured $T_{m,Cl}$ using the method described in (Collins, 1979). The T_{h-tot} provided minimum temperatures associated with different stages of ore-forming fluid evolution. Salinity is quantified as the weight percentage of NaCl equivalent (wt %NaCl eqv.) (Fan et al., 2006).

4.3 *In-situ* analysis of trace elements in pyrite

The *in-situ* analysis of pyrite was conducted using LA-ICP-MS at Wuhan Sample Solution Analytical Technology Co., Ltd., Wuhan, China. The operating conditions and data reduction for laser ablation systems and ICP-MS instruments were performed as described by (Zong et al., 2017). Laser sampling was carried out using the GeolasPro laser ablation system, which comprised a MicroLas optical system and a COMPexPro 102 ArF excimer laser (maximum energy of 200 mJ and wavelength of 193 nm). Ion signal intensities were acquired using the Agilent 7,700e ICP-MS instrument. Helium served as the carrier gas while argon acted as the supplementary gas; both gases were mixed prior to entering ICP. A “wire” signal smoothing device (Hu et al., 2015) was also incorporated into the laser ablation system. The spot frequency and size of the laser were set at 5 Hz and 32 μm , respectively. The elemental compositions of pyrite was calibrated using various reference materials (NIST 610 and NIST 612) without the use of an internal standard (Liu et al., 2008). The sulfide reference material MASS-1 (USGS) was utilized as the unknown sample to validate the calibration method's accuracy. Each analysis included a 20s–30s background acquisition followed by 50s of data acquisition from the sample. The off-line selection and integration of background and analyzed signals, time-drift correction, and quantitative calibration for trace element analysis were performed using an Excel-based software called ICPMSDataCal (Liu et al., 2008).

4.4 *In-situ* analysis of S isotope in pyrite

The *in-situ* S isotope analysis of pyrite was conducted using the Neptune Plus MC-ICP-MS (Thermo Fisher Scientific, Bremen, Germany) equipped with a Geolas HD excimer ArF laser ablation system (Coherent, Gottingen, Germany) at Wuhan Sample Solution Analytical Technology Co., Ltd., Wuhan, China. Helium was employed as the carrier gas for the laser ablation system. To mitigate potential sulfur isotope ratio downhole fractionation effects during analysis (Fu et al., 2016), we opted for a large beam spot size

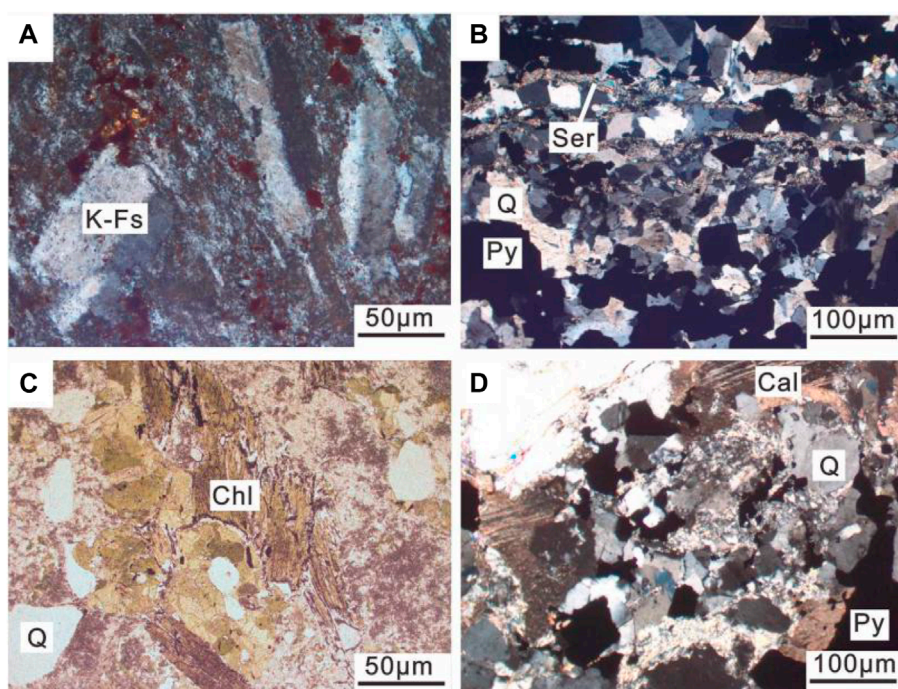


FIGURE 9 Typical photos of wall rock alterations in the Zhaoxian gold deposit; (A) Potassic alteration in wall rock (+), K-feldspar is the representative mineral. (B) Beresitization in wall rock (+), the representative minerals are pyrite, quartz and sericite. (C) Chloritization in wall rock (-), amphibole and biotite in the andesite altered by chlorite. (D) Carbonitization in wall rock (+), representative mineral is calcite. Abbreviations: Cal = calcite, Chl = chlorite, K-Fs = K-feldspar, Py = pyrite, Q = quartz, Ser = sericite.

(44 μm), low frequency (2 Hz) laser conditions, and performed approximately 100 laser pulses per single analysis. Additionally, a signal smoothing device (Hu et al., 2021) was utilized to ensure stable signals under slow frequency conditions. The fixed laser energy density was set at 5.0 J/cm². Equipped with 9 Faraday cups and 10¹¹ Ω resistance amplifiers, the Neptune Plus employed L3, C, and H3 Faraday cups for simultaneous static reception of ³²S, ³³S, and ³⁴S signals. A high-performance Jet + X cone combination was used to enhance signal strength. Nitrogen gas (4 mL/min) was introduced into the plasma to minimize polyatomic ion interference. Medium-resolution modes (~5,000) were adopted for data acquisition purposes. Pyrite samples were calibrated against pyrite standard PPP-1 to avoid the matrix effect, and reference values of δ³⁴S_{v-CDT} were obtained from previous work (Fu et al., 2016). All analyzed data underwent processing using professional isotope data processing software “ISO-Compass” (Zhang et al., 2020).

5 Results

5.1 BSE images of minerals

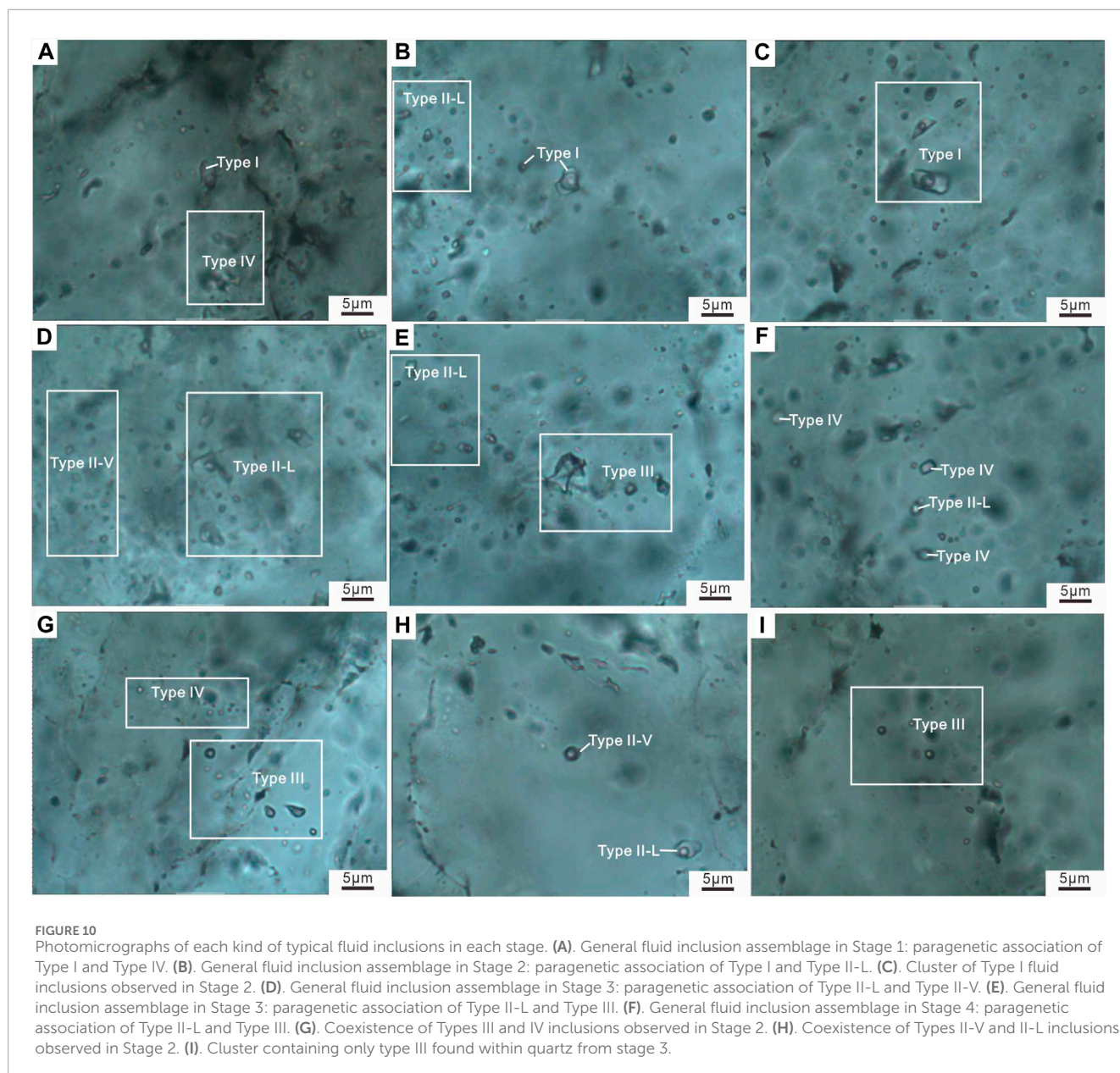
In the Zhaoxian gold deposit, pyrite was identified as the predominant and significant sulfide and gold-bearing mineral throughout all stages of ore formation (Figures 6, 7). Native gold was also frequently observed in the Zhaoxian gold deposit, exhibiting diameters ranging from 2 μm to 30 μm. It displayed a distinct bright golden yellow color and commonly occurred as

inclusions or within fissures under reflected light or BSE images (Figures 6B, C, 7B). Other metallic minerals such as chalcopyrite, galena, and sphalerite were also present (Figures 6E, 7C). Gangue minerals including quartz, sericite, chlorite, and K-feldspar were predominantly observed but on a smaller scale compared to sulfides and quartz.

The SEM-BSE image of Py1 primarily exhibits idiomorphic to hypidiomorphic grains without an oscillating zone (Figure 7A). Py2 exhibits idiomorphic to hypidiomorphic grains with mineral inclusions such as chalcopyrite and natural gold present. Oscillating zones are visible in Py2 indicating a relatively volatile formation environment (Figure 7B). In contrast, oscillating zones and mineral inclusions were not observed in Py3, while sulfides (e.g., chalcopyrite and galena) often filled the fissures of Py3 suggesting stable physical and chemical conditions during this stage (Figure 7C). Finally, Py4 appears as hemidiomorphic grains with minimal cracks or mineral inclusion without any oscillating zones (Figure 7D).

5.2 Petrographic characteristics of fluid inclusion

The acidic environment in the ore-forming fluid can enhance the stability of metal complexes, which facilitate the transportation of gold and other elements involved in ore formation through various types of complexes (Yang, 1986; Phillips and Evans, 2004; Hou et al., 2007; Lu, 2011; Mao et al., 2013). The properties of



ore-forming fluids can be directly elucidated by measuring the homogenization temperature and salinity of fluid inclusion. In our research of quartz veins in the Zhaoxian gold deposit, we have identified and classified four types of fluid inclusion (Figure 10): CO₂-rich inclusion (Type I), biphasic aqueous inclusion (Type II), monophasic gaseous inclusion (Type III), and monophasic aqueous inclusion (Type IV).

Type I inclusion: CO₂-rich inclusion, primarily consists of NaCl, H₂O, CO₂, and CH₄, with a diameter ranging from 3 μm to 17 μm (Figures 10A–C). These inclusions exhibit an elliptical or irregular shape and display in many styles: three phases (clathrate, liquid CO₂, and gas CO₂), biphasic (clathrate, liquid CO₂), monophasic (liquid or gas CO₂).

Type II inclusion is predominantly composed of NaCl solution (liquid) phase and bubble (gaseous) phase, with a diameter ranging

from 2 μm to 12 μm (Figures 10B, D–F, H), accounting for the largest proportion. These inclusions display elliptical, linear, irregular, and negative crystalline features. They are commonly found in conjunction with other inclusions and occur across all metallogenic stages. Based on their vapor/liquid ratios (VLRs), these inclusions can be further classified into liquid-rich (Type II-L) and vapor-rich (Type II-V). Type II-L inclusions exhibit VLRs ranging from 10% to 50% at room temperature, whereas Type II-V inclusions exhibit VLRs ranging from 50% to 90% at room temperature.

Type III inclusion consists primarily of gaseous carbon dioxide with traces of methane or water vapor (Figures 10E, G, I). They have a diameter range of 4 μm–10 μm. Type III inclusion exhibits irregular shapes. These inclusions are present in all stages of the ore formation process.

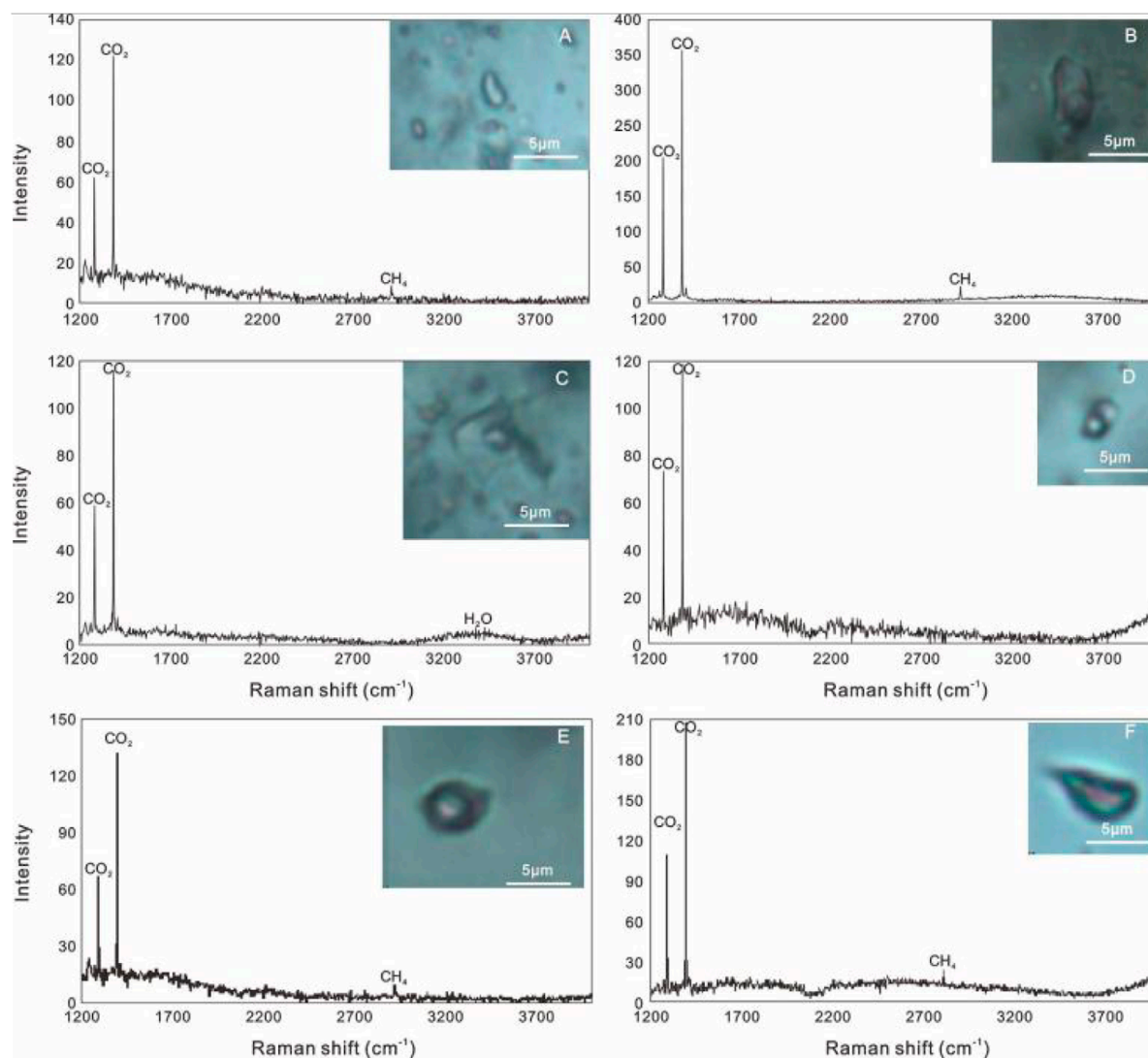


FIGURE 11

Representative Raman spectra of fluid inclusions in quartz. (A). Monophase Type I inclusions, containing CO₂ and CH₄ in liquid form. (B). The gas phase of three-phase Type I inclusions, containing CO₂ and CH₄. (C). The gas phase of Type II-L inclusions, containing CO₂ and H₂O. (D). The gas phase of Type II-L inclusions, containing only CO₂. (E). The gas phase of Type II-V inclusions, containing CO₂ and H₂O. (F). The gas phase of Type III inclusions, containing CO₂ and CH₄.

Type IV inclusion is primarily aqueous inclusion, with a diameter range of 4 μm–10 μm (Figures 10A, E, G). They exhibit an irregular shape. Type IV inclusion can be observed across all stages of ore formation.

5.3 Laser Raman spectroscopy

The compositions of the volatile component of fluid inclusions were determined by micro-laser Raman spectroscopy analysis on representative samples from each stage (Figure 11). Type I inclusions exhibit distinct peaks of CO₂ and CH₄ in either the vapor or clathrate phase (Figures 11A, B). Type II inclusions show a prominent CO₂ peak (Figures 11C–E), H₂O peak (Figure 11C), and CH₄ peak (Figure 11E). Type III inclusions at

each stage display noticeable CO₂ and CH₄ peaks (Figure 11F). Laser Raman spectrum analysis has confirmed that the ore-forming fluid consists of an H₂O–NaCl–CO₂–CH₄ system (Figure 11).

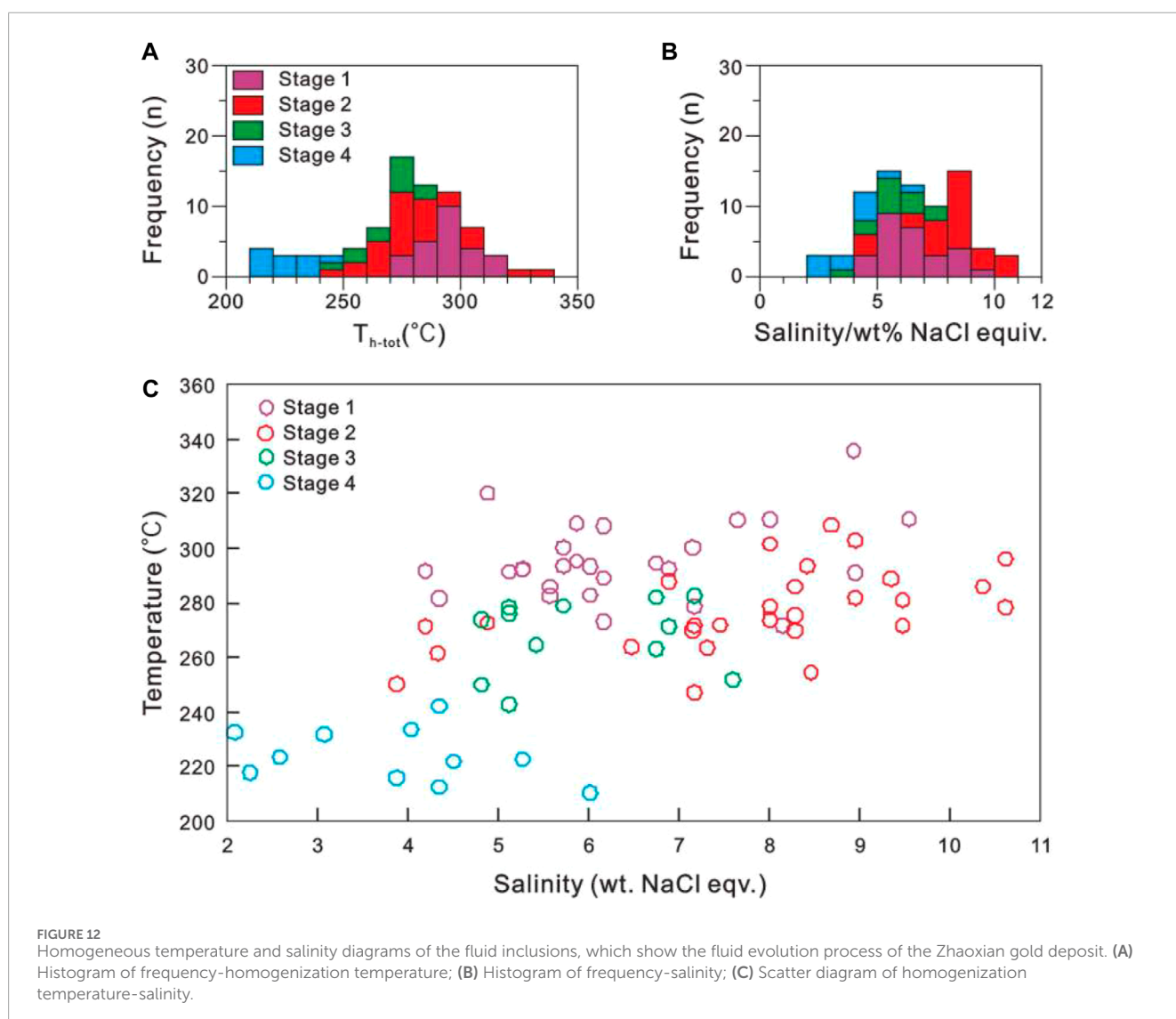
5.4 Microthermometry analysis

Microthermometry analysis of fluid inclusion in quartz from different stages in Zhaoxian gold deposit has been carried out (Table 1; Figure 12).

In Stage 1, the milky quartz vein primarily contains two types of inclusion: types I and II. Unfortunately, the T_{m,CO_2} for Type I inclusion are unavailable due to their small volume. The final melting temperature of $T_{m,cl}$ ranges from 4.7°C to 7.5°C,

TABLE 1 Microthermometry results of fluid inclusions in the Zhaoxian gold deposit.

Stage	Type	T_{m, CO_2} (°C)	$T_{m, Cl}$ (°C)	T_{h, CO_2} (°C)	T_{m-ice} (°C)	T_{h-tot} (°C)	Salinity (wt%)
Stage 1	1	unavailable	4.7–7.5	25–29	not applicable	300–336	4.9–9.5
	2	not applicable	not applicable	not applicable	–5.8 to –2.5	272–311	4.2–9.0
Stage 2	1	–58 to –57	5.4–7.8	26–28	not applicable	255–273	4.3–8.5
	2	not applicable	not applicable	not applicable	–7.1 to –2.3	247–308	3.9–10.6
Stage 3	2	not applicable	not applicable	not applicable	–4.8 to –2.9	243–283	4.8–7.6
Stage 4	2	not applicable	not applicable	not applicable	–3.7 to –1.2	210–242	2.1–6.0



and the T_{h, CO_2} ranges from 25°C to 29°C. The majority of these inclusions completely homogenized into the liquid phase, while a minority of them homogenized into the gas phase. The T_{h-tot} ranges from 300°C to 336°C, and the salinity ranges

from 4.9 wt% NaCl eqv to 9.5 wt% NaCl eqv. As for Type II inclusion, after undergoing complete freezing and subsequent warming, the T_{m-ice} ranging from –5.8°C to –2.5°C, while the T_{h-tot} ranges from 272°C to 311°C. Additionally, the calculated

salinity varies between 4.2 wt% NaCl eqv. and 9.0 wt% NaCl eqv. Most of Type II have undergone complete homogenization into the liquid phase, while only a minority have transitioned into the gas phase.

In Stage 2, a large number of primary fluid inclusions were discovered in smoky quartz veins. The predominant inclusion species in this stage is Type II, with Type I also being commonly observed, while Types 3 and 4 appear to be present in smaller quantities. For Type I inclusion, the T_{m,CO_2} ranges from -58°C to -57°C , the $T_{m,Cl}$ ranges from 5.4°C to 7.8°C , and the T_{h,CO_2} ranges from 26°C to 28°C . In this stage, the quantity of Type I inclusion that homogenized into the gas phase surpasses that observed in Stage 1. The T_{h-tot} of the Type I inclusion ranges from 255°C to 273°C , the salinity of which ranges from 4.3 wt% NaCl eqv. to 8.5 wt% NaCl eqv. For Type II inclusion, the T_{m-ice} of the Type II inclusion ranges from -7.1°C to -2.3°C , the T_{h-tot} ranges from 247°C to 308°C and the calculated salinity ranges from 3.9 wt% NaCl eqv. to 10.6 wt% NaCl eqv. The quantity of inclusion homogenized into the gas phase at this stage is also higher compared to Stage 1.

In Stage 3, the dominant fluid inclusion in smoky gray quartz veins mainly consists of Type II, with a small amount of types III and IV. The T_{m-ice} of the Type II inclusion ranges from -4.8°C to -2.9°C , the T_{h-tot} ranges from 243°C to 283°C , and the calculated salinity ranges from 4.8 wt% NaCl eqv. to 7.6 wt% NaCl eqv.

In Stage 4, the dominant fluid inclusion in smoky gray quartz veins mainly consists of types II and IV. The T_{m-ice} of the Type II inclusion ranges from -3.7°C to -1.2°C . The T_{h-tot} , and calculated salinity of Type II inclusion in Stage 4 is significantly lower compared to earlier stages, ranging from 210°C to 242°C and 2.1 wt% NaCl eqv to 6.0 wt% NaCl eqv, respectively.

5.5 Trace element distribution in pyrite

Regarding the distribution of trace elements in pyrite, Table 2; Figures 13, 14 present the analytical results for each stage.

The size of Py1 is smaller than the beam spot applied for LA-ICP-MS analysis.

The Py2 sample exhibits significant variations in Au and As content, with the highest Au content observed among all stages. In Py2, each stage demonstrates the highest content of Ga, Sn, Sb, W, and Tl; whereas Co, Ni, Cu, Zn, Ag, and In exhibit the lowest content. Distinct zones of Au-As-Cu enrichment and depletion can be identified within Py2, indicating the presence of oscillating regions, other elements generally exist in solid solution with their contents showing a horizontal trend corresponding to ablation depth (Figures 14A, B).

The Py3 sample exhibits elevated levels of Ag and base metal elements, including Cu, Zn, Cd, In, Pb, and Bi. However, the contents of Co and Ni are comparatively higher in Py3 compared to Py2. Additionally, polymetallic sulfide inclusions become prevalent in Py3 samples; this phenomenon suggests the precipitation of polymetallic sulfides from the ore-forming fluid (Figures 14C, D).

Except for Co and Ni which have equal content to that in Py2, the content of Py4 is significantly lower than that observed in both Py2 and Py3. Other elements generally exist in solid solution with their contents showing a horizontal trend corresponding to ablation

depth, and their contents are generally the lowest among all stages (Figures 14E, F).

5.6 Sulfur isotope composition in pyrite

Table 3 and Figure 15 present the sulfur isotope composition in pyrite of Zhaoxian gold deposit. The $\delta^{34}\text{S}$ values of Py2 range from $+10.51\text{‰}$ to $+11.01\text{‰}$, with an average value of $+10.75\text{‰}$; for Py3, the $\delta^{34}\text{S}$ values range from $+9.56\text{‰}$ to $+10.10\text{‰}$, with an average value of $+9.80\text{‰}$; and for Py4, the $\delta^{34}\text{S}$ values range from $+12.02\text{‰}$ to $+12.44\text{‰}$, with an average value of $+12.18\text{‰}$.

6 Discussion

6.1 Characteristics and evolution of deep ore-forming fluids

In the discussion, we examine the characteristics and evolution of deep ore-forming fluids. Previous studies have investigated the ore-forming fluids of gold deposits in the Jiaodong gold province and have found that they are characterized by medium temperatures (200°C – 400°C) and low salinity (0 wt% NaCl eqv.–10 wt% NaCl eqv.) (Fan et al., 2003; Wen et al., 2016; Liu et al., 2019; Hu et al., 2021; Wu et al., 2022). The fluid inclusion composition primarily consists of H_2O -NaCl- $\text{CO}_2 \pm \text{CH}_4$.

Researchers have also studied the fluid system of gold deposits in the Sanshandao gold belt and found similarities with the Jiaodong gold district. Specifically, the ore-forming fluids at shallow depths (100 m–600 m below sea level) show similarities between the Jiaodong gold district and the Sanshandao gold belt. In this study, we focus on the ore-forming fluids at depths ranging from 1,731 m to 1,372 m below sea level in the Zhaoxian gold deposit.

It is worth noting that CH_4 has been generally detected in this study. Previous work suggests that CH_4 often appears in the main ore stage at a depth ranging from 2,146 m to 2,038 m below sea level (Li et al., 2023). In this study, it can be found that CH_4 is common in the Type I fluid inclusion of Stage 2. The possible sources of CH_4 in hydrothermal fluids previous study summarized are fluid-rock interaction (Berndt et al., 1996; Potter et al., 1998; 2004; Cao et al., 2014), the mantle (Abrajano et al., 1988; Kendrick et al., 2011), or biological processes (Des-Marais et al., 1988; Ueno et al., 2006). The fluid inclusion in the samples collected from gold deposits below 3,000 m in the Sanshandao gold belt has been extensively investigated; however, no presence of CH_4 was detected in these samples (Wen et al., 2016). This implies that the mantle source and biological source are unlikely to be responsible for the CH_4 in this district, as there is no sedimentary stratum present. We propose that a fluid-rock interaction involving hornblende, ilmenite, and plagioclase in the wall rock with the ore-forming fluid may have been the initial source of CH_4 in both Sanshandao and Jiaojia gold belt gold deposits. Therefore, the most likely source of CH_4 can be attributed to a fluid-rock interaction wherein hornblende, ilmenite, and plagioclase in the host rock underwent reactions with the ore-forming fluid, resulting in the formation of sphene and liberation

TABLE 2 The LA-ICP-MS analysis results of pyrite in different stages of the Zhaoxian gold deposit (ppm).

	Co	Ni	Cu	Zn	Ga	Ge	As	Se	Mo	Ag
20Zx23-1-01	4.17	14.4	28.1	1.98	0.48	0.35	16.1	11.2	0.02	5.80
20Zx23-1-02	0.16	0.99	14.3	3.19	0.26	0.62	23.5	0.00	0.00	3.65
20Zx23-1-03	1.37	2.15	14.5	43.5	0.56	0.82	18.1	0.00	0.02	3.65
20Zx23-1-04	0.95	4.18	7.00	2.84	0.20	0.42	1457.1	7.15	0.00	0.86
20Zx23-1-05	4.57	8.58	1.87	6.06	0.22	0.19	1547.5	5.68	0.00	0.29
20Zx23-1-06	2.36	6.85	7.99	1.61	0.07	0.96	201.1	0.00	0.02	2.12
20Zx23-1-07	1.40	4.41	17.9	1.76	0.21	0.91	657.0	8.68	0.02	3.68
20Zx23-1-08	1.38	5.82	25.7	3.85	0.62	0.54	19.7	12.5	0.03	5.51
20Zx23-1-09	0.57	0.88	19.4	42.4	0.12	0.87	9.04	0.00	0.00	4.31
20Zx23-1-10	4.97	7.53	5.25	2.30	0.13	0.61	1196.4	0.00	0.24	0.67
20Zx37-2-01	633.4	20.1	3727.0	47.5	0.03	1.80	197.5	7.44	0.02	4.03
20Zx37-2-02	221.4	32.5	1270.5	31.1	0.09	0.75	115.9	8.29	0.00	4.68
20Zx37-2-03	82.2	30.9	337.7	12.2	0.04	0.24	194.4	0.00	0.00	14.6
20Zx37-2-04	360.5	21.2	1172.7	13.2	0.05	0.23	106.1	0.00	0.00	3.05
20Zx37-2-05	332.9	21.7	1826.2	27.8	0.12	0.22	131.8	0.00	0.03	5.87
20Zx37-2-06	201.6	28.3	341.6	15.0	0.00	0.30	140.0	0.00	0.05	15.3
20Zx37-2-07	232.6	33.2	2007.3	17.9	0.00	0.48	198.2	6.25	0.00	4.18
20Zx37-2-08	431.8	24.4	1611.5	17.4	0.10	0.24	137.8	5.16	0.00	2.78
20Zx37-2-09	255.8	26.6	1296.4	24.7	0.13	0.11	218.2	0.00	0.00	4.96
20Zx37-2-10	83.6	11.6	134.3	16.1	0.00	0.01	113.0	0.03	0.01	4.63
20Zx43-2-01	592.8	51.0	1.89	2.52	0.00	0.64	52.1	5.24	0.04	0.24
20Zx43-2-02	148.1	45.9	0.00	2.01	0.10	0.16	28.3	0.00	0.00	0.05
20Zx43-2-03	119.3	21.4	0.18	2.42	0.09	0.43	21.1	4.46	0.02	0.01
20Zx43-2-04	896.3	35.9	0.54	2.33	0.10	0.74	87.4	8.77	0.00	0.03
20Zx43-2-05	1615.5	13.5	0.25	1.06	0.01	0.55	74.7	6.57	0.00	0.00
20Zx43-2-06	99.4	11.1	0.34	2.65	0.06	0.32	52.6	0.00	0.00	0.00
20Zx43-2-07	84.4	6.89	0.00	2.11	0.00	0.35	57.1	6.66	0.00	0.00
20Zx43-2-08	84.4	6.84	0.25	1.26	0.01	0.34	68.0	0.00	0.00	0.00
20Zx43-2-09	58.8	43.9	0.11	2.46	0.00	1.07	61.2	15.4	0.00	0.02
20Zx43-2-10	103.9	50.4	0.18	1.40	0.12	0.38	44.9	0.00	0.00	0.05

(Continued on the following page)

TABLE 2 (Continued) The LA-ICP-MS analysis results of pyrite in different stages of the Zhaoxian gold deposit (ppm).

	Cd	In	Sn	Sb	W	Pt	Au	Tl	Pb	Bi
20Zx23-1-01	0.00	0.00	0.16	19.4	0.31	0.00	0.33	0.18	410.4	0.01
20Zx23-1-02	0.00	0.00	0.25	8.12	0.03	0.01	0.33	0.09	184.8	0.01
20Zx23-1-03	0.17	0.01	0.00	10.1	0.23	0.02	0.28	0.09	184.1	0.01
20Zx23-1-04	0.00	0.02	0.14	19.5	0.04	0.05	1.86	0.16	77.0	0.08
20Zx23-1-05	0.00	0.00	0.29	0.92	0.01	0.01	2.09	0.00	11.5	0.00
20Zx23-1-06	0.08	0.00	0.00	5.97	0.70	0.00	0.56	0.09	117.2	0.00
20Zx23-1-07	0.00	0.01	0.14	10.1	0.02	0.00	1.44	0.04	221.4	0.03
20Zx23-1-08	0.00	0.01	0.04	16.3	0.07	0.00	0.13	0.17	296.3	0.00
20Zx23-1-09	0.00	0.00	0.05	17.2	0.01	0.00	0.25	0.06	284.1	0.00
20Zx23-1-10	0.00	0.00	0.00	8.03	3.05	0.00	2.62	0.05	81.1	0.01
20Zx37-2-01	0.34	0.20	0.04	5.77	0.01	0.04	0.27	0.06	2197.4	13.1
20Zx37-2-02	0.15	0.11	0.00	4.27	0.06	0.00	0.38	0.01	576.3	15.5
20Zx37-2-03	0.45	0.03	0.00	7.24	0.86	0.01	0.40	0.05	13,528.7	47.3
20Zx37-2-04	0.00	0.09	0.02	2.19	0.01	0.01	0.24	0.01	741.8	9.81
20Zx37-2-05	0.05	0.22	0.00	2.64	0.06	0.00	0.21	0.03	3442.6	20.2
20Zx37-2-06	0.41	0.06	0.02	5.77	0.01	0.00	0.48	0.07	13,508.0	42.4
20Zx37-2-07	0.15	0.13	0.03	5.51	0.01	0.02	0.48	0.05	441.0	17.9
20Zx37-2-08	0.05	0.14	0.06	1.85	0.00	0.02	0.23	0.02	543.0	8.63
20Zx37-2-09	0.37	0.20	0.20	4.57	0.00	0.00	0.43	0.02	1507.8	18.8
20Zx37-2-10	0.31	0.03	0.00	3.97	0.05	0.01	0.29	0.03	1299.7	16.0
20Zx43-2-01	0.00	0.00	0.01	0.05	0.17	0.00	0.31	0.01	4.11	16.3
20Zx43-2-02	0.06	0.00	0.00	0.02	0.00	0.00	0.01	0.00	0.12	0.17
20Zx43-2-03	0.00	0.00	0.08	0.04	1.37	0.00	0.03	0.00	0.40	1.86
20Zx43-2-04	0.07	0.00	0.03	0.04	0.00	0.06	0.01	0.01	0.27	0.62
20Zx43-2-05	0.00	0.00	0.17	0.00	0.16	0.02	0.00	0.00	0.07	0.21
20Zx43-2-06	0.20	0.00	0.03	0.01	0.00	0.01	0.01	0.01	0.46	0.20
20Zx43-2-07	0.00	0.00	0.18	0.01	0.01	0.00	0.01	0.00	0.02	0.12
20Zx43-2-08	0.07	0.00	0.05	0.05	0.01	0.01	0.02	0.01	0.61	1.05
20Zx43-2-09	0.09	0.00	0.00	0.00	0.00	0.07	0.01	0.00	0.84	0.04
20Zx43-2-10	0.00	0.00	0.00	0.00	0.01	0.00	0.01	0.00	0.69	2.18

of hydrogen gas. The hydrogen further catalyzed the reduction of CO₂ to CH₄ (Wen et al., 2016; Hu et al., 2021). Consequently, the alteration of the wall rock adjacent to the orebodies at depths ranging

from 1,731 m to 1,372 m below sea level may exhibit a higher degree of intensity compared to that observed at depths ranging from 2,146 m to 2,038 m below sea level.

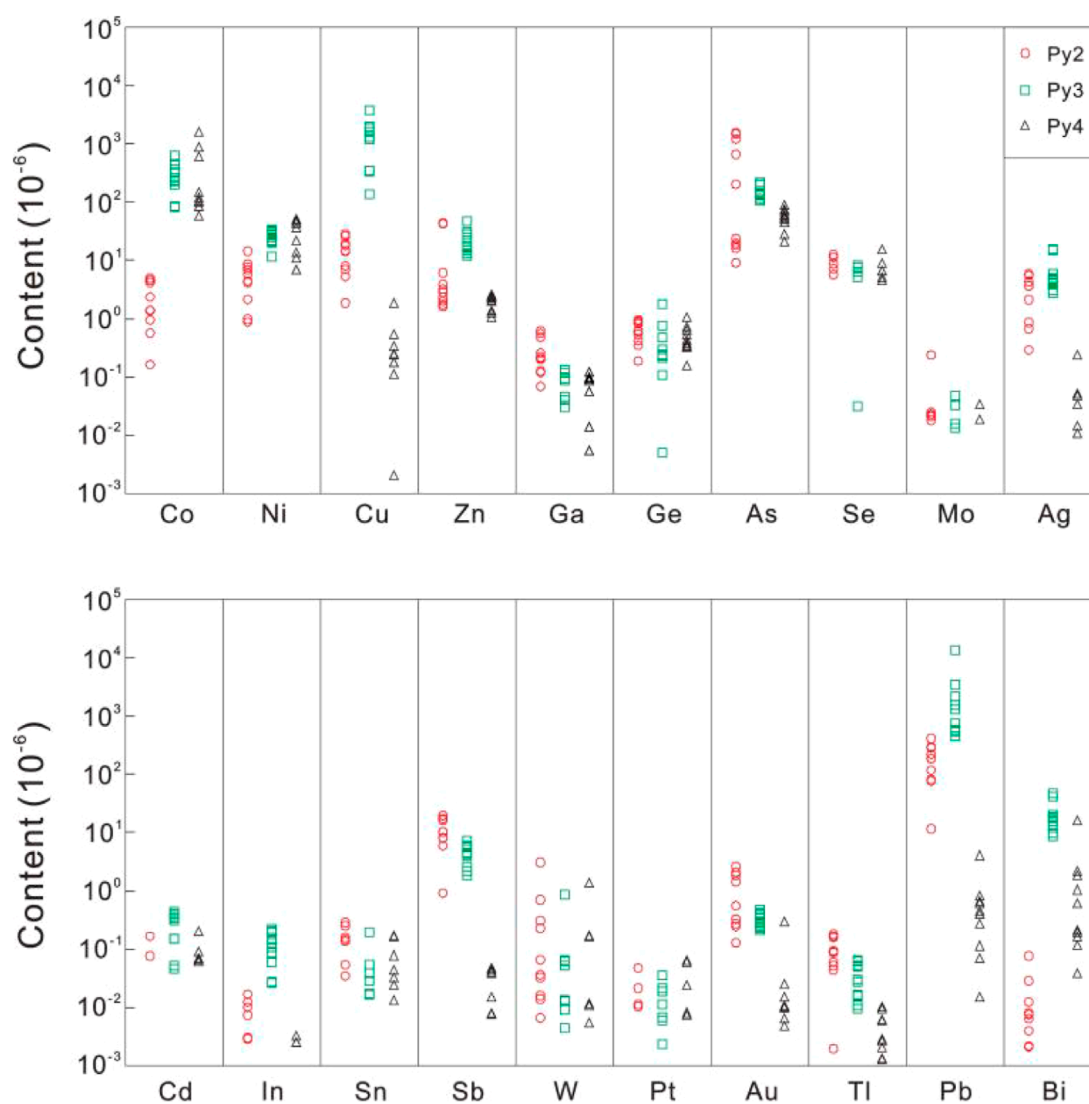


FIGURE 13
Comparison of the content of the trace elements among different stages in the Zhaoxian gold deposit.

The ore-forming fluid system in the Zhaoxian gold deposit is characterized as a medium-temperature (210°C–336°C) and moderate-low salinity (3.9 wt% NaCl eqv.–10.6 wt% NaCl eqv.) system. We have compiled and analyzed temperature and salinity data (Figure 12) from various stages of fluid inclusion. It was observed that the ore-forming temperature and salinity generally decreased from earlier to later stages. In Stage 1 veins, the ore-forming fluids may be primary magmatic water released from magma. The fluid inclusions in Stage 1 primarily consist of Type I and Type II inclusions, with Type I accounting for the largest percentage among all stages (25%), while Type II accounts for 75%. In Stage 2, the salinity data can be divided into two clusters, while the temperature remains relatively constant. Furthermore, the simultaneous presence of liquid-rich Type II inclusion and Type III inclusion can be observed in various microscopic regions within quartz sections of Stage 2. In Stage 2, the fluid inclusions consist of Type I inclusion (10%), Type II inclusion (65%), Type III inclusion (25%), with Type IV being insignificantly present.

These phenomena potentially indicate the occurrence of fluid boiling. However, the predominant sight within quartz during Stages 3 and 4 is an abundance of liquid-rich type II inclusion. Homogeneous temperatures and salinities exhibited by these stages' fluid inclusions suggest a stable mineralizing process. In Stage 3, fluids include type I (5%), type II (80%), type III (5%), and type IV (10%). In Stage 4, fluids include Type II (80%) and Type IV (20%). It is hypothesized that decreases in temperature and pressure are the primary factors influencing the precipitation of each element. Gas phase analysis through laser Raman spectrum reveals composition mainly consisting of CO₂, CH₄, and H₂O. The homogenization temperature appears similar, suggesting a distinct composition of the H₂O-CO₂ fluid phase during gold and pyrite precipitation, implying fluid boiling. Cooling can induce instability in metal complexes within the ore-forming fluid, leading to gold precipitation. In stages 3 and 4, a gradual decrease in both the homogeneous temperature and salinity of fluid inclusion is observed, with relatively minor variations in salinity. Additionally,

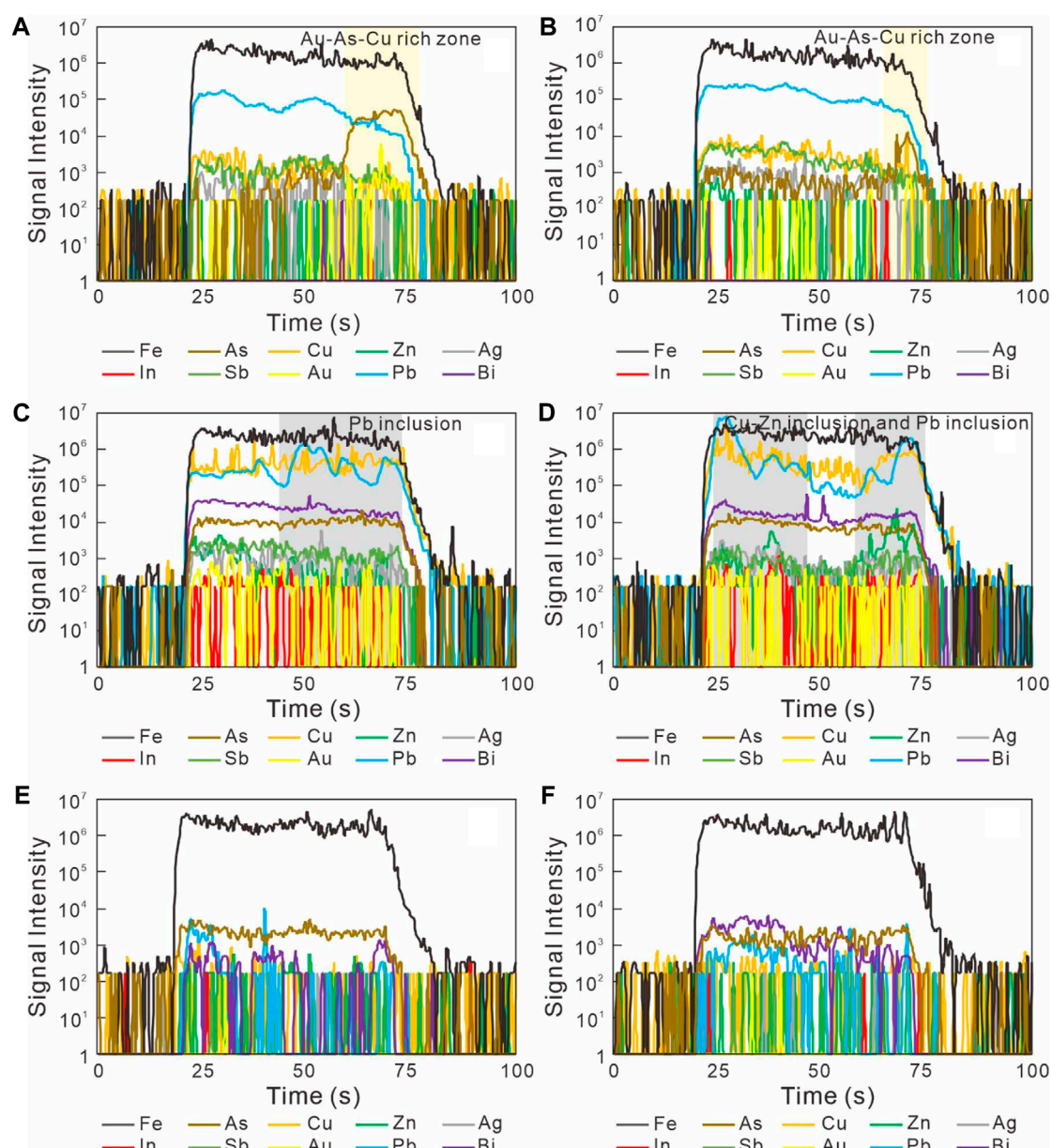


FIGURE 14

(A, B) The representative LA-ICP-MS time-resolved depth profiles of Py2 exhibit zones rich in Au-As-Cu. (C, D) The representative LA-ICP-MS time-resolved depth profiles of Py3 reveal the presence of sulfide inclusions. (E, F) The representative LA-ICP-MS time-resolved depth profiles of Py4 demonstrate the occurrence of trace elements often found in solid solution.

the presence of CH_4 in fluid inclusion suggests a contribution of fluids from fluid-rock interaction.

In the Zhaoxian gold deposit, the metallogenic process follows a similar evolution trend to most gold deposits in the Jiaodong gold district, but there are differences in ore-forming temperature and salinity range. As the fluid moves upward, there is a decrease in pressure, which can result in phase separation (Hu et al., 2021). This phase separation is significant in the partitioning of elements during fluid chemistry evolution (Ulrich et al., 2002; Klemm et al., 2007; 2008; Landtwing et al., 2010) and can lead to fluid boiling. There is also a slight change in salinity (Figure 12),

with salinity decreasing with stage, depth, and temperature, possibly due to fluid-rock interaction and decompressing effect. Overall, it is believed that the Jiaodong gold province has a unified ore-forming fluid system. The Sanshandao gold belt and Jiaojia gold belt have similar ore-forming fluid properties, dominated by $\text{H}_2\text{O}-\text{NaCl}-\text{CO}_2 \pm \text{CH}_4$, with medium temperature and medium-low salinity characteristics. Metal precipitation in these systems is caused by decompression, cooling, phase separation, fluid mixing, and fluid-rock interaction. Fluid boiling and fluid-rock interactions are likely important mechanisms of mineralization.

TABLE 3 The LA-MC-ICP-MS Sulfur isotopic composition of different stages of pyrite in the Zhaoxian gold deposit.

Sample name	$\delta^{34}\text{S}_{\text{V-CDT}}$ (‰)	Delta-2SE
ZX23-1-01	11.01	0.05
ZX23-1-02	10.82	0.04
ZX23-1-03	10.72	0.05
ZX23-1-04	10.51	0.04
ZX23-1-05	10.70	0.04
ZX37-2-01	9.95	0.05
ZX37-2-02	10.10	0.05
ZX37-2-03	9.82	0.06
ZX37-2-04	9.56	0.06
ZX37-2-05	9.56	0.05
ZX43-2-01	12.02	0.05
ZX43-2-02	12.44	0.04
ZX43-2-03	12.04	0.05
ZX43-2-04	12.23	0.04
ZX43-2-05	12.19	0.04

6.2 Evaluation of the elements in pyrite from three stages (Py2–Py4)

Recent studies have shown that Au, Ag, As, and heavy metals can enter the pyrite lattice through solid solutions or mineral inclusion at the micron to nanometer scale (Reich et al., 2005; Deditius et al., 2008; 2009; 2011; Barker et al., 2009; Large et al., 2009). The examination of pyrite not only enhances our understanding of the characteristics and distribution of metals, but also provides insights into the underlying processes governing mineralization events such as hydrothermal alteration, metamorphism, and deformation (Reich et al., 2005; 2016; Cook et al., 2009; Thomas et al., 2011; Deditius et al., 2014; Peterson and Mavrogenes, 2014; Steadman et al., 2015; Meffre et al., 2016).

In Stage 2 (Py2), the gold content is observed to be the highest compared to other stages, as determined by *in-situ* analysis of trace elements in pyrite. The variations in gold and arsenic content in Py2 indicate a clear positive correlation between these two elements, suggesting their formation as a distinct element group during this stage. Oscillating zones enriched in gold have been identified, indicating rapid decompression and the presence of volatile substances that trigger sudden changes in the chemical environment of the fluid (Large et al., 2009; Muntean et al., 2011; Steadman et al., 2015; Gregory et al., 2016; Tardani et al., 2017). Morphologically, the porous structure of pyrite particles (Simon et al., 1999) and abundance of mineral micro-inclusions (such as chalcocopyrite; Figure 5D) suggest fluid boiling (Román et al.,

2019). High-temperature elements such as Ga, Sn, Sb, W, and Tl exhibit higher concentrations compared to other stages while Co, Ni, Cu, Zn, Ag, and In show lower concentrations (Figures 13, 17). However, there exists a negative relationship between (Ag, Cu, Pb, Sb) and Au whereas positive relationships are observed among these four elements (Figure 16). By cross-referencing the primary data, we have identified the presence of these elements in a solid solution, which has been documented in several research studies (e.g., Large et al., 2007; Large et al., 2009; Román et al., 2019). Oscillating zones and sulfide inclusions can be readily identified in the SEM-BSE image of Py2 grains (Figure 7B), the Au-As-Cu enrich and deplete zones within Py2 (Figures 14A, B) is also an evidence, thus implying that fluid boiling mechanisms are involved in ore formation. We noticed that Au exist in native gold grains (Figures 5C, 6B, 6C, 7B), while in the Au vs. As diagram (Figure 16A), all data points fall below the Au saturation line indicating potential undersaturation of gold within ore-forming fluids (Reich et al., 2005), considering the enrichment of native gold in this stage, this suggesting that the ore-forming fluid in this stage saturated at the beginning, the precipitation of native gold led to the unsaturation of Au in later fluids and Py2.

In Stage 3 (Py3), the concentrations of Ag, Cu, Zn, In, Pb, and Bi exhibit the highest contents among all stages (Figures 13, 17). Furthermore, the contents of Co and Ni are higher in Py3 compared to Py2. A relatively weaker positive correlation can be observed between Au, Sb, and Bi contents (Figures 16G, H). Additionally, a significant positive correlation is observed between the element groups (Ag, Pb, Sb, and Bi) and (Cu, Zn, and In), indicating extensive involvement of polymetallic sulfides (Figure 17). Furthermore, the coexistence of chalcocopyrite, galena, and sphalerite in the fissures in Py3 and quartz further supports this opinion. Significant Pb-(Zn) inclusions were detected in Py3 (Figures 14C, D), along with the corresponding BSE image (Figure 7C) showed that chalcocopyrite and galena are common in pyrite grains and fissures, indicating the precipitation of multiple polymetallic sulfides during this stage.

In Stage 4 (Py4), it appears that the chemical properties of the ore-forming fluid have reached a state of equilibrium. The formation of Py4 occurred through a tranquil process, with other sulfides being scarce in Stage 4. The pyrite content in stage 4 (Py4) is significantly lower compared to stages 2 and 3 (Py2 and Py3), except for Co and Ni, which exhibit similar levels as Py2 (Figures 13, 17). A relatively weak positive correlation can be observed between Zn, Pb, Sb, and Bi content in Py4. This suggests that stage 4 represents the final phase of ore formation, with most elements having undergone nearly complete precipitation from the ore-forming fluid. The occurrence of trace elements in Py4 often found in pyrite solid solution, few sulfide inclusions was found (Figures 14E, F).

The substitution of Fe^{2+} in pyrite with Co^{2+} and Ni^{2+} is favored by an increase in $f\text{S}_2$ and/or a decrease in temperature (Maslennikov et al., 2009). As gold and polymetallic sulfide gradually precipitates from the ore-forming fluid at each stage, without any supplementary source, the $f\text{S}_2$ should be decreasing. Therefore, an increase in Co and Ni contents (Figure 13) would indicate a decrease in temperature. This is coincide with the result of fluid inclusion microthermometry analysis (Figure 12).

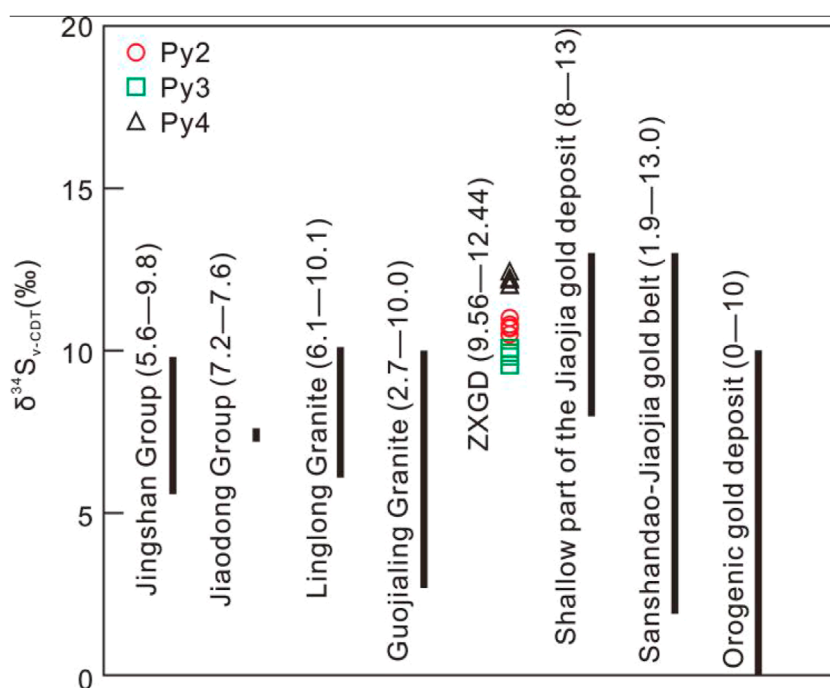


FIGURE 15
 Comparison of the content of the trace elements among different stages in the Zhaoxian gold deposit. Sulfur isotope contrast diagram was constructed for the Jingshan group (Mao et al., 2008), Jiaodong group (Mao et al., 2008), Linglong granite (Yang, 1998), Guojialing granite (Li et al., 1993), Jiaojia shallow mineralization (Mills et al., 2015), Sanshandao–Jiaojia gold metallogenic belt (Deng et al., 2015; Yang et al., 2017), and orogenic gold deposits worldwide (Goldfarb et al., 2005).

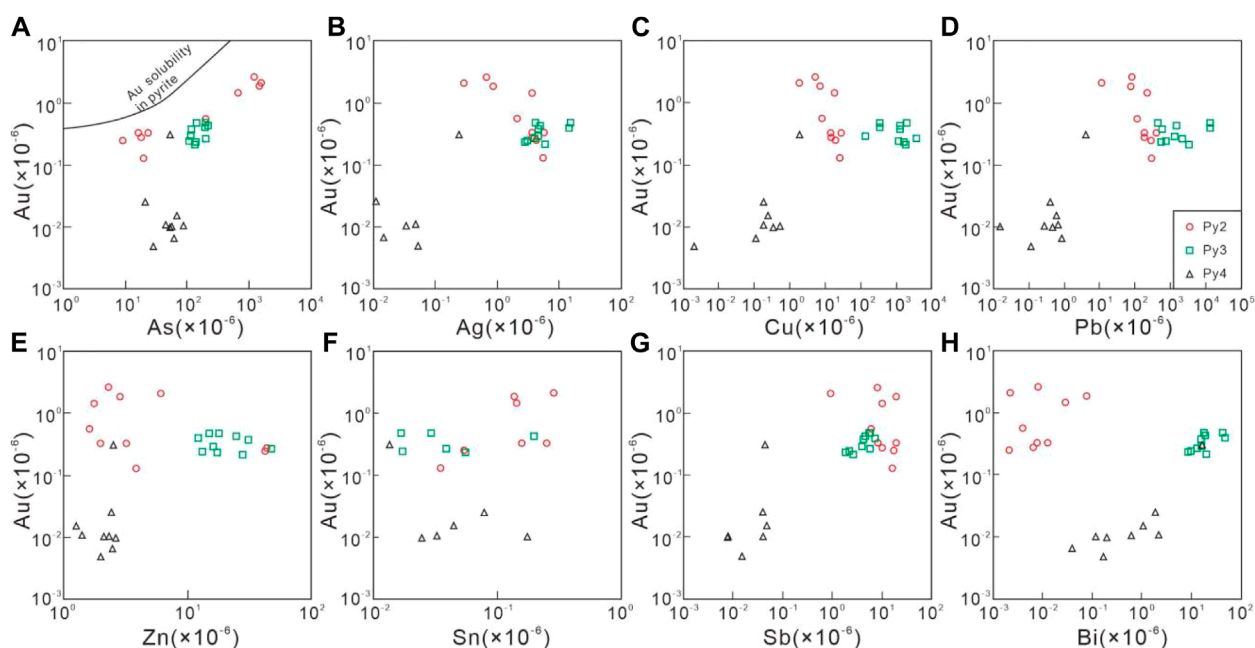
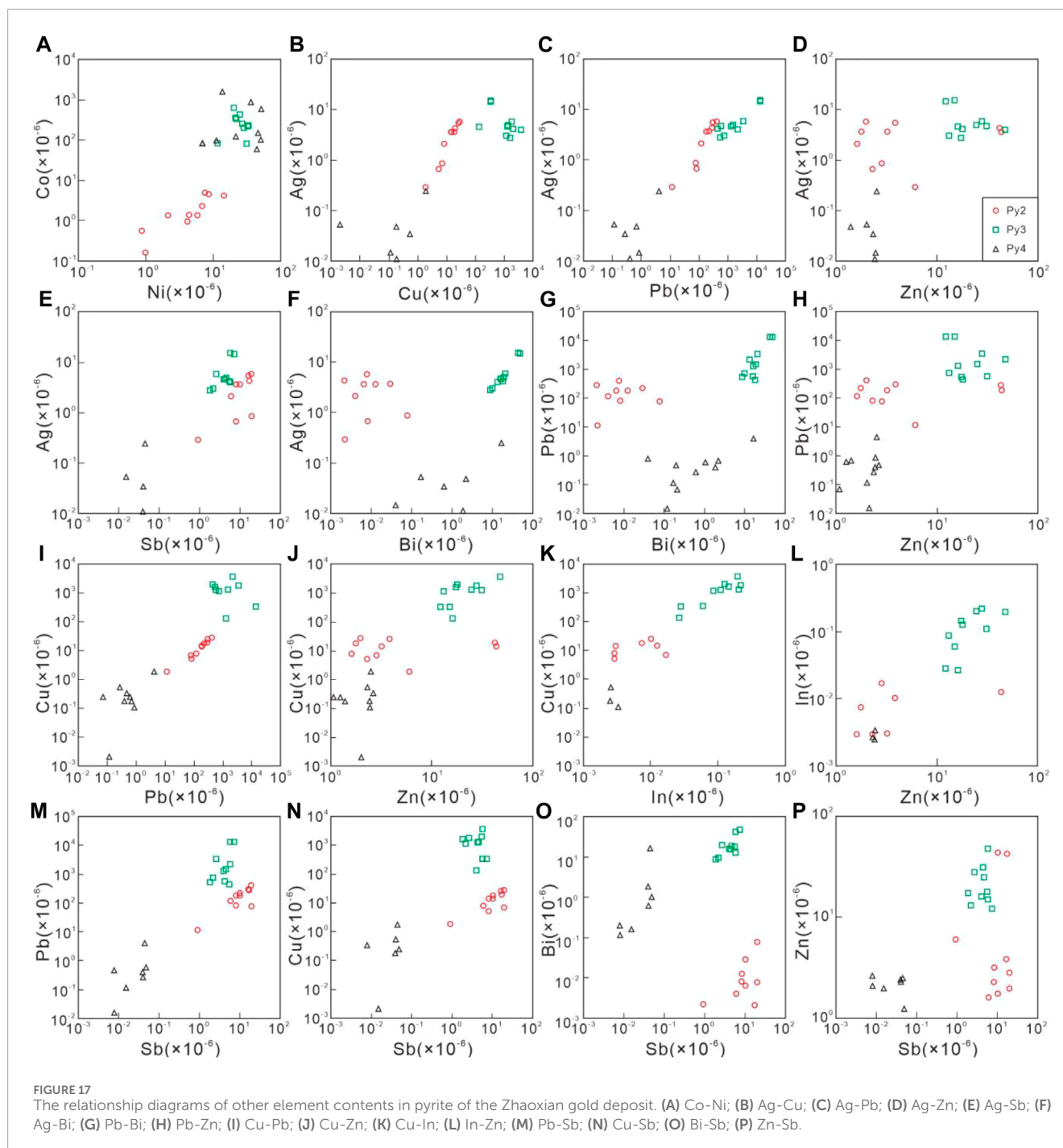


FIGURE 16
 The relationship diagrams of Au and some element contents in pyrite of the Zhaoxian gold deposit. (A) Au-As; (B) Au-Ag; (C) Au-Cu; (D) Au-Pb; (E) Au-Zn; (F) Au-Sn; (G) Au-Sb; (H) Au-Bi.

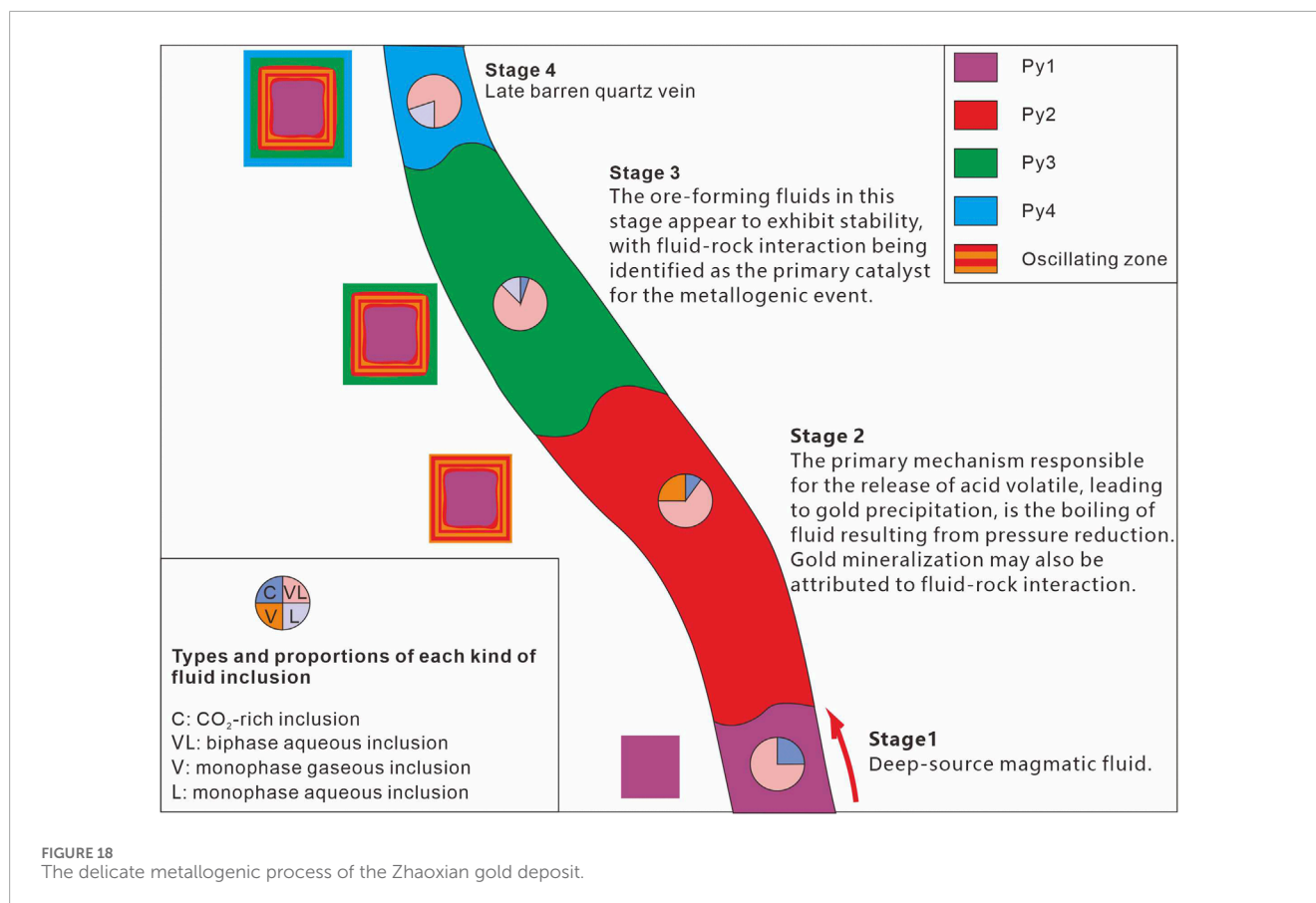


6.3 The sulfur isotopic values of pyrite from three stages

The $\delta^{34}\text{S}$ values of pyrite from each stage in the Zhaoxian gold deposit exhibit similarity, ranging from +10.51‰ to +11.01‰ for Py2, +9.56‰ to +10.10‰ for Py3, and +12.02‰ to +12.44‰ for Py4, with mean values of +10.75‰, +9.80‰, and +12.18‰ respectively (Figure 15). The $\delta^{34}\text{S}$ values of the Zhaoxian gold deposit are comparable to those of Jiaojia gold deposit (shallow part, 8‰–13‰) and Sanshandao-Jiaojia gold belt (+1.9‰ to +13.0‰),

while a little higher than those of Linglong granitoid (+6.1‰ to +10.1‰) and the Guojialing granitoid (+2.7‰ to +10.0‰), indicating a medium-to-low temperature system without significant isotopic fractionation.

Therefore, there may exist certain disparities in the characteristics of the ore-forming fluids during each stage, albeit originating from a common source. Fluid-rock interactions could potentially contribute to the elevation of $\delta^{34}\text{S}$ values. As the ore-forming fluids ascended, modifications in temperature, pressure, and oxygen or sulfide fugacity would likely occur. Findings



from fluid inclusion studies propose that Au precipitation might primarily occur through fluid boiling, while multiple sulfides could precipitate via fluid-rock interactions. These processes are predominantly chemical in nature and relatively unaffected by external materials. Furthermore, the $\delta^{34}\text{S}$ values of Zhaoxian gold deposit overlap with those observed in the Jiaojia gold district at depths around -300 m (Mills et al., 2015), ranging from $+8\%$ to $+13\%$. This implies that the shallower portion of the ore-forming fluids shares a similar origin with its deeper counterpart.

In conclusion, it can be inferred that the primary ore-forming fluid in the Zhaoxian gold deposit is most likely to be magmatic-hydrothermal fluids. Moreover, considering the occurrence of orebodies within surrounding rocks, it is plausible that the ore-forming fluid has undergone extensive reactions with the host rock, potentially resulting in some sulfur inheritance from these surrounding rocks.

6.4 Delicate metallogenic process of Zhaoxian gold deposit

Stage 1 is characterized by a deep-source magmatic fluid, exhibiting high temperature and salinity, along with a predominant presence of Type I fluid inclusion (25%, the highest proportion among all stages) (Figure 18). The occurrence of idiomorphic-hypautomorphic pyrite grains indicates a thermally stable fluid environment.

Stage 2 is the most crucial stage for gold mineralization in Zhaoxian gold deposit, providing compelling evidence of fluid boiling through the coexistence of liquid-rich Type II and Type III fluid inclusions, significant variations in salinity while maintaining a relatively constant temperature, oscillating zones, and the concomitant variations and fluctuations in the concentrations of Au and As (Figure 18, Zhang et al., 2023). Fluid boiling plays a crucial role in the formation of magmatic-hydrothermal gold deposits (Brown, 1986; Seward, 1989). During this process, $\text{Au}(\text{HS})_2$ may be the most significant form of gold transformation under low-temperature and neutral conditions (Stefansson and Seward, 2004). The release of H_2S not only leads to a sharp decrease in the concentration of dissolved gold but also controls the evolution of sulfide and oxide complexes. These processes facilitate gas escape and result in an increased concentration of metal elements. Furthermore, medium-low salinity fluids rich in CO_2 and H_2O may be released during the evolution of mantle-derived magma (Ridley and Diamond, 2000). CO_2 functions as a regulator of gold solubility while maintaining stability within a specific range for Au-S complexes (Liu and Shen, 1999). This facilitates the generation of vapor in gaseous form, ultimately leading to a reduction in pressure and an elevation in fluid pH upon its evaporation (Lowenstern et al., 1991). Additionally, CH_4 was detected in the gas phase of the inclusion during Stage 2, while wall-rock alteration, including potassic alteration, sericitization, chloritization, and carbonatization, can be observed in the ores (Figure 4B). This suggests that fluid-rock interaction also plays a significant role in gold precipitation by influencing the pH of

ore-forming fluids through CO₂ mineral reactions (Khedr et al., 2013; 2023; Abdelkarim et al., 2022). As the ore-forming fluid ascends, it inevitably interacts with surrounding rocks leading to changes. During this stage, gold primarily exists as native gold and solid-solution within the pyrite lattice. The presence of elevated levels of Ga, Sn, Sb, W, and Tl in the ore indicates high temperatures during ore formation as indicated by fluid inclusion analysis results. Concentrations of Ag, Cu, Pb, and Sb often exhibit a positive correlation, the representative LA-ICP-MS time-resolved depth profiles suggesting their existence may be solid forms within pyrite (the signals of these elements almost remain horizontal, Figures 14A, B). These micro-inclusions further indicate a process of fluid boiling.

Stage 3 is the primary polymetallic stage in the Zhaoxian gold deposit. The dominant type of fluid inclusion is Type II, which is rich in water. The temperature, salinity, and trace element content in pyrite (Py3) appear to be stable, and the salinity is relatively low. Additionally, CH₄ has been detected in the gas phase of the fluid inclusion in Stage 3, and alterations in the surrounding rock can be observed in the ores. This suggests that fluid-rock interaction plays a significant role in the precipitation of polymetallic minerals. An oscillating zone can hardly be found in Py3, chalcopyrite, sphalerite, and galena filled in the fissures of Py3 and quartz, this can also be proved in the representative LA-ICP-MS time-resolved depth profiles (Figures 14C, D). In this aspect, Py3 is the precipitant of polymetallic sulfides. Therefore, the ore-forming fluids in this stage seem to be stable, the most important inducer of the metallogenic event is fluid-rock interaction (Figure 18). In this stage, multiple sulfides precipitate from the ore-forming fluids, with Cu, Zn, Ag, Cd, In, Pb and Bi showing the highest concentrations among all stages. The precipitation temperatures of these elements are generally lower than that of gold, indicating a decrease in temperature, which is consistent with the data from fluid inclusion analysis.

Stage 4 is primarily characterized by late barren quartz veins (Figure 18) which generally have the lowest homogeneous temperature and salinity of fluid inclusion among all stages. Similarly, the trace element content (except Co and Ni) in pyrite (Py4) is also the lowest among all stages, they exist in pyrite solid solution (Figures 14E, F).

7 Conclusion

- (1) We have classified the process of ore formation into four stages: Stage 1 - barren quartz vein with fine-grained pyrite (early stage), Stage 2 - quartz-pyrite-native gold (gold stage), Stage 3 - quartz-polymetallic sulfide±native gold (polymetallic stage), and Stage 4 - quartz-calcite±pyrite (late stage).
- (2) The gold in the Zhaoxian gold deposit primarily occurs as native gold grains, while a minor portion is present in solid solution within pyrite.
- (3) During the gold stage, fluid boiling occurs, while the chemical properties of ore-forming fluid in the polymetallic sulfide stage remain stable.
- (4) The ore-forming fluid of the Zhaoxian gold deposit is medium temperature, medium to low salinity, H₂O-NaCl-CO₂-CH₄ fluid system.

- (5) The δ³⁴S values of pyrite in Zhaoxian gold deposit are similar to those found in gold deposits in the Jiaojia gold belt and higher than the Linglong granite and Guojialing granite. This suggests that the ore-forming fluid in Jiaodong gold deposits may have originated from magmatic-hydrothermal processes, fluid-rock interaction may also happened during the metallogenic process.

Data availability statement

The original contributions presented in the study are included in the article/Supplementary material, further inquiries can be directed to the corresponding author.

Author contributions

ZZ: Conceptualization, Investigation, Writing-original draft. QZ: Conceptualization, Funding acquisition, Investigation, Supervision, Visualization, Writing-review and editing. H-RF: Funding acquisition, Investigation, Supervision, Writing-review and editing. RB: Investigation, Resources, Writing-review and editing. JW: Funding acquisition, Investigation, Writing-review and editing. XL: Investigation, Writing-review and editing. YZ: Investigation, Writing-review and editing. LH: Resources, Writing-review and editing.

Funding

The author(s) declare financial support was received for the research, authorship, and/or publication of this article. This work was financially supported by Shandong Engineering Research Center of Application and Development of Big Data for Deep Gold Exploration Open Project "Applying multiproxy techniques for the comprehensive prediction of the ultra-deep gold deposits from the Jiaojia gold belt, Shandong province" (No. SKD202215) and the National Key R & D Program of China "Development and utilization of strategic mineral resources" (Grant No. 2023YFC2906900).

Acknowledgments

We are grateful to reviewers for constructive suggestions. We express our gratitude to the engineers from Shandong Gold Geology and Mineral Exploration Co., Ltd. For their invaluable assistance in facilitating the sampling process.

Conflict of interest

Author ZZ was employed by Sinosteel Overseas Resources Limited. Author RB was employed by Shandong Gold Geology and Mineral Exploration Co., Ltd.

The remaining authors declare that the research was conducted in the absence of any commercial or financial relationships that could be construed as a potential conflict of interest.

Publisher's note

All claims expressed in this article are solely those of the authors and do not necessarily represent those of their affiliated

organizations, or those of the publisher, the editors and the reviewers. Any product that may be evaluated in this article, or claim that may be made by its manufacturer, is not guaranteed or endorsed by the publisher.

References

- Abdelkarim, A. A. M., Elawady, A., Khedr, M. Z., Elafandy, A. H., Elwan, W., Tamura, A., et al. (2022). Genesis of sulfide mineralization, atshan and darhib areas, south eastern desert of Egypt: evidence of fluid pathway effects along shear zones. *Arab. J. Sci. Eng.* 47 (1), 641–665. doi:10.1007/s13369-021-05736-y
- Abrajano, T. A., Sturchio, N. C., Bohlke, J. K., Lyon, G. L., Poreda, R. J., and Stevens, C. M. (1998). Methane-hydrogen gas seeps, Zambales ophiolite, Philippines: deep or shallow origin? *Chem. Geol.* 71, 211–222. doi:10.1016/0009-2541(88)90116-7
- Barker, S. L. L., Hickey, K. A., Cline, J. S., Dipple, G. M., Kilburn, M. R., Vaughan, J. R., et al. (2009). Unlocking invisible gold: use of NanoSIMS to evaluate gold, trace elements, and sulfur isotopes in pyrite from carlin-type gold deposits. *Econ. Geol.* 104 (7), 897–904. doi:10.2113/econgeo.104.7.897
- Berndt, M. E., Allen, D. E., and Seyfried, W. E. (1996). Reduction of CO₂ during serpentinization of olivine at 300 °C and 500 bar. *Geology* 24, 351–354. doi:10.1130/0091-7613(1996)024<0351:rocdso>2.3.co;2
- Bodnar, R. J. (1993). Revised equation and table for determining the freezing point depression of H₂O–NaCl solutions. *Geochim. Cosmochim. Acta* 57, 683–684. doi:10.1016/0016-7037(93)90378-A
- Brown, K. L. (1986). Gold deposition from geothermal discharges in New Zealand. *Econ. Geol.* 81 (4), 979–983. doi:10.2113/gsecongeo.81.4.979
- Cai, Y. C., Fan, H. R., Santosh, M., Hu, F. F., Yang, K. F., and Li, X. H. (2018). Decratonic gold mineralization: evidence from the Shangzhuang gold deposit, eastern North China Craton. *Gondwana Res.* 54, 1–22. doi:10.1016/j.gr.2017.09.009
- Cao, M. J., Qin, K. Z., Li, G. M., Evans, N. G., and Jin, L. Y. (2014). Abiogenic Fischer–Tropsch synthesis of methane at the Baogutu reduced porphyry copper deposit, western Junggar, NW China. *Geochim. Cosmochim. Acta* 141, 179–198. doi:10.1016/j.gca.2014.06.018
- Collins, P. L. F. (1979). Gas hydrates in CO₂-bearing fluid inclusions and the use of freezing data for estimation of salinity. *Econ. Geol.* 74, 1435–1444. doi:10.2113/gsecongeo.74.6.1435
- Cook, N. J., Ciobanu, C. L., and Mao, J. W. (2009). Textural control on gold distribution in as-free pyrite from the dongping, huangtuliang and hougou gold deposits, north China craton (hebei province, China). *Chem. Geol.* 264 (1–4), 101–121. doi:10.1016/j.chemgeo.2009.02.020
- Deditius, A. P., Reich, M., Kesler, S. E., Utsunomiya, S., Chryssoulis, S. L., Walshe, J., et al. (2014). The coupled geochemistry of Au and as in pyrite from hydrothermal ore deposits. *Geochim. Cosmochim. Acta* 140, 644–670. doi:10.1016/j.gca.2014.05.045
- Deditius, A. P., Utsunomiya, S., Ewing, R. C., Chryssoulis, S. L., Venter, D., and Kesler, S. E. (2009). Decoupled geochemical behavior of as and Cu in hydrothermal systems. *Geology* 37 (8), 707–710. doi:10.1130/g25781a.1
- Deditius, A. P., Utsunomiya, S., Reich, M., Kesler, S. E., Ewing, R. C., Hough, R., et al. (2011). Trace metal nanoparticles in pyrite. *Ore Geol. Rev.* 42 (1), 32–46. doi:10.1016/j.oregeorev.2011.03.003
- Deditius, A. P., Utsunomiya, S., Renock, D., Ewing, R. C., Ramana, C. V., Becker, U., et al. (2008). A proposed new type of arsenian pyrite: composition, nanostructure and geological significance. *Geochim. Cosmochim. Acta* 72 (12), 2919–2933. doi:10.1016/j.gca.2008.03.014
- Deng, J., Liu, X., Wang, Q., and Pan, R. (2015). Origin of the Jiaodong-type Xinli gold deposit, Jiaodong Peninsula, China: constraints from fluid inclusion and C–D–O–S–Sr isotope compositions. *Ore Geol. Rev.* 65, 674–686. doi:10.1016/j.oregeorev.2014.04.018
- Deng, J., Yang, L. Q., Groves, D. I., Zhang, L., Qiu, K. F., and Wang, Q. F. (2020). An integrated mineral system model for the gold deposits of the giant Jiaodong province, eastern China. *Earth-Sci. Rev.* 208, 103274. doi:10.1016/j.earscirev.2020.103274
- Des-Marais, D. J., Stallard, M. L., Nehring, N. L., and Truesdell, A. H. (1988). Carbon isotope geochemistry of hydrocarbons in the Cerro Prieto geothermal field, Baja California Norte, Mexico. *Mex. Chem. Geol.* 71, 159–167. doi:10.1016/0009-2541(88)90112-X
- Dong, C. Y., Wang, S. J., Liu, D. Y., Wang, J. G., Xie, H. Q., Wang, W., et al. (2010). Late Palaeoproterozoic crustal evolution of the North China craton and formation time of the Jingshan Group: constraints from SHRIMP U–Pb zircon dating of meta-intermediate–basic intrusive rocks in eastern Shandong province. *Acta Petrol. Sin.* 27, 1699–1706. (in Chinese with English abstract).
- Fan, H. R., Feng, K., Li, X. H., Hu, F. F., and Yang, K. F. (2016). Mesozoic gold mineralization in the Jiaodong and Korean peninsulas. *Acta Petrol. Sin.* 32 (10), 3225–3238. (in Chinese with English abstract).
- Fan, H. R., Hu, F. F., Yang, J. H., Shen, K., and Zhai, M. G. (2007). Fluid evolution and large scale gold metallogeny during Mesozoic tectonic transition in the eastern Shandong province. *Geol. Soc. Lond. Spec. Publ.* 21 (5), 1317–1328. (in Chinese with English abstract).
- Fan, H. R., Hu, F. F., Yang, J. H., and Zhai, M. G. (2007). Fluid evolution and large-scale gold metallogeny during Mesozoic tectonic transition in the Jiaodong Peninsula, eastern China. *Geol. Soc. Lond. Spec. Publ.* 280 (1), 303–316. doi:10.1144/SP280.16
- Fan, H. R., Hu, F. F., Yang, K. F., and Wang, K. Y. (2006). Fluid unmixing/immiscibility as an ore forming process in the giant REE–Nb–Fe deposit, Inner Mongolian, China: evidence from fluid inclusions. *J. Geochem. Explor.* 89, 104–107. doi:10.1016/j.gexplo.2005.11.039
- Fan, H. R., Zhai, M. G., Xie, Y. H., and Yang, J. H. (2003). Ore-forming fluids associated with granite-hosted gold mineralization at the Sanshandao deposit, Jiaodong gold province, China. *Min. Deposita* 38 (6), 739–750. doi:10.1007/s00126-003-0368-x
- Feng, K., Fan, H. R., Hu, F. F., Yang, K. F., Liu, X., Shangguan, Y. N., et al. (2018). Involvement of anomalously As–Au-rich fluids in the mineralization of the Heilan'gou gold deposit, Jiaodong, China: evidence from trace element mapping and *in-situ* sulfur isotope composition. *J. Asian Earth Sci.* 160, 304–321. doi:10.1016/j.jseas.2017.12.023
- Fu, J. L., Hu, Z. C., Zhang, W., Yang, L., Liu, Y. S., Li, M., et al. (2016). *In situ* sulfur isotopes ($\delta^{34}\text{S}$ and $\delta^{33}\text{S}$) analyses in sulfides and elemental sulfur using high sensitivity cones combined with the addition of nitrogen by laser ablation MC–ICP–MS. *Anal. Chim. Acta* 911, 14–26. doi:10.1016/j.aca.2016.01.026
- Goldfarb, R. J., Baker, T., Dube, B., Groves, D. I., Hart, C. J. R., and Gosselin, P. (2005). Distribution, character, and genesis of gold deposits in metamorphic terran. *Econ. Geol.* 100th Anniv., 407–450. doi:10.5382/AV100.14
- Goldfarb, R. J., and Groves, D. I. (2015). Orogenic gold: common or evolving fluid and metal sources through time. *Lithos* 233, 2–26. doi:10.1016/j.lithos.2015.07.011
- Goldfarb, R. J., and Santosh, M. (2014). The dilemma of the Jiaodong gold deposits: are they unique? *Geosci. Front.* 5, 139–153. doi:10.1016/j.gsf.2013.11.001
- Goss, S. C., Wilde, S. A., Wu, F., and Yang, J. (2010). The age, isotopic signature and significance of the youngest Mesozoic granitoids in the Jiaodong Terrane, Shandong Province, North China Craton. *Lithos* 120 (3–4), 309–326. doi:10.1016/j.lithos.2010.08.019
- Gregory, D. D., Large, R. R., Bath, A. B., Steadman, J. A., Wu, S., Danyushevsky, L., et al. (2016). Trace element content of pyrite from the kapai slate, st. Ives gold district, western Australia. *Econ. Geol.* 111 (6), 1297–1320. doi:10.2113/econgeo.111.6.1297
- Groves, D. I., Santosh, M., Deng, J., Wang, Q. F., Yang, L. Q., and Zhang, L. (2020). A holistic model for the origin of orogenic gold deposits and its implications for exploration. *Min. Deposita* 55 (2), 275–292. doi:10.1007/s00126-019-00877-5
- Hou, M. L., Jiang, S. Y., Shen, K., Lian, G. J., Liu, Q. C., and Xiao, F. L. (2007). Geochemistry of fluid inclusions and hydrogen and oxygen isotopes in Penglai gold mining area. *Jiaodong. Acta Petrol. Sin.* 9, 2241–2256. (in Chinese with English abstract).
- Hu, H. L., Jiang, X. H., Liang, G. Z., Yang, K. F., and Fan, H. R. (2021). The vertical variation characteristics of ore-forming fluids of the Jiaojia deposit: implications for mineralizing processes of gold deposits in the Jiaodong peninsula. *Bull. Mineral. Petrol. Geochem.* 40, 1–12. (in Chinese with English abstract). doi:10.19658/j.issn.1007-2802.2021.40.053
- Hu, Z. C., Zhang, W., Liu, Y. S., Gao, S., Li, M., Zong, K. Q., et al. (2015). “Wave” signal smoothing and mercury-removing device for laser ablation quadrupole and multiple collector ICPMS analysis: application to lead isotope analysis. *Anal. Chem.* 87 (2), 1152–1157. doi:10.1021/ac503749k
- Jahn, B. M., Liu, D. Y., Wan, Y. S., Song, B., and Wu, J. J. (2008). Archean crustal evolution of the Jiaodong Peninsula, China, as revealed by zircon SHRIMP geochronology elemental and Nd–isotope geochemistry. *Am. J. Sci.* 308 (3), 232–269. doi:10.2475/03.2008.03
- Jiang, N., Chen, J. Z., Guo, J. H., and Chang, G. H. (2012). *In situ* zircon U–Pb, oxygen and hafnium isotopic compositions of Jurassic granites from the North China Craton: evidence for Triassic subduction of continental crust and subsequent metamorphism-related 18O depletion. *Lithos* 142–143, 84–94. doi:10.1016/j.lithos.2012.02.018

- Kendrick, M. A., Honda, M., Walshe, J., and Petersen, K. (2011). Fluid sources and the role of abiogenic-CH₄ in Archean gold mineralization: constraints from noble gases and halogens. *Precambrian Res.* 189, 313–327. doi:10.1016/j.precamres.2011.07.015
- Khedr, M. Z., Desouky, A. A. A., Kamh, S., Hauzenberger, C., Arai, S., Tamura, A., et al. (2023). Petrogenesis of Gerf Neoproterozoic carbonatized peridotites (Egypt): evidence of convergent margin metasomatism of depleted sub-arc mantle. *Lithos*, 450–451. doi:10.1016/j.lithos.2023.107192
- Khedr, M. Z., Kamh, S., Desouky, A. A. A., Takazawa, E., Hauzenberger, C., Whattam, S. A., et al. (2013). Remote sensing and geochemical investigations of sulfide-bearing metavolcanic and gabbroic rocks (Egypt): constraints on host-rock petrogenesis and sulfide genesis. *Gondwana Res.* 119, 282–312. doi:10.1016/j.gr.2023.03.021
- Klemm, L. M., Pettke, T., and Heinrich, C. A. (2008). Fluid and source magma evolution of the Questa porphyry Mo deposit, New Mexico, USA. *Min. Deposita* 43 (5), 533–552. doi:10.1007/s00126-008-0181-7
- Klemm, L. M., Pettke, T., Heinrich, C. A., and Campos, E. (2007). Hydrothermal evolution of the El Teniente deposit, Chile: porphyry Cu-Mo ore deposition from low-salinity magmatic fluids. *Econ. Geol.* 102 (6), 1021–1045. doi:10.2113/gsecongeo.102.6.1021
- Landtwing, M. R., Furrer, C., Redmond, P. B., Pettke, T., Guillon, M., and Heinrich, C. A. (2010). The bingham canyon porphyry Cu-Mo-Au deposit. III. Zoned copper-gold ore deposition by magmatic vapor expansion. *Econ. Geol.* 105 (1), 91–118. doi:10.2113/gsecongeo.105.1.91
- Large, R. R., Danyushevsky, L., Hollit, C., Maslennikov, V., Meffre, S., Gilbert, S., et al. (2009). Gold and trace element zonation in pyrite using a laser imaging technique: implications for the timing of gold in orogenic and Carlin-Style sediment-hosted deposits. *Econ. Geol.* 104 (5), 635–668. doi:10.2113/gsecongeo.104.5.635
- Large, R. R., Maslennikov, V. V., Robert, F., Danyushevsky, L. V., and Chang, Z. (2007). Multistage sedimentary and metamorphic origin of pyrite and gold in the giant sukhoi log deposit, Lena Gold Province, Russia. *Econ. Geol.* 102 (7), 1233–1267. doi:10.2113/gsecongeo.102.7.1233
- Li, B., Peng, Y. M., Zhao, X. Y., Liu, X. N., Wang, G. W., Jiang, H. W., et al. (2022). Combining 3D geological modeling and 3D spectral modeling for deep mineral exploration in the zhaoxian gold deposit, Shandong province, China. *Minerals* 12 (10), 1272. doi:10.3390/min12101272
- Li, H. Q., Liu, J. Q., and Wei, L. (1993). *Chronological study of fluid inclusion for hydrothermal deposit and its geological applications*. Beijing: Geological publishing house, 1–126. (In Chinese).
- Li, L., Santosh, M., and Li, S.-R. (2015). The 'Jiaodong type' gold deposits: characteristics, origin and prospecting. *Ore Geol. Rev.* 65, 589–611. doi:10.1016/j.oregeorev.2014.06.021
- Li, Q., Song, H., Chi, G. X., Zhang, G. Y., and Xu, Z. Q. (2021). Genesis of visible gold in pyrite in the Zhaoxian gold deposit, Jiaodong gold province, China: constraints from EBSD micro-structural and LA-ICP-MS elemental analyses. *Ore Geol. Rev.* 139, 104591. doi:10.1016/j.oregeorev.2021.104591
- Li, X. C., Fan, H. R., Santosh, M., Hu, F. F., Yang, K. F., Lan, T. G., et al. (2012). An evolving magma chamber within extending lithosphere: an integrated geochemical, isotopic and zircon U-Pb geochronological study of the Gushan granite, eastern North China Craton. *J. Asian Earth Sci.* 50, 27–43. doi:10.1016/j.jseas.2012.01.016
- Li, X. H., Fan, H. R., Hu, F. F., Hollings, P., Yang, K. F., and Liu, X. (2019). Linking lithospheric thinning and magmatic evolution of late Jurassic to early cretaceous granitoids in the Jiaobei Terrane, southeastern North China Craton. *Lithos* 324–325, 280–296. doi:10.1016/j.lithos.2018.11.022
- Li, Z., Mao, G. Z., Liu, C. J., Liu, X. T., An, P. R., and Cao, M. P. (2023). Nature and geochemical characteristics of ore-forming fluids in the Zhaoxian gold deposit, Jiaodong gold province, eastern China. *Front. Earth Sci.* 10, 1085398. doi:10.3389/feart.2022.1085398
- Liu, B., and Shen, K. (1999). *Thermodynamics of fluid inclusions*. Beijing: China: Geological Publishing House.
- Liu, S., Hu, R. Z., Gao, S., Feng, C. X., Yu, B. B., Qi, Y. Q., et al. (2009). Zircon U-Pb age, geochemistry and Sr-Nd-Pb isotopic compositions of adakitic volcanic rocks from Jiaodong, Shandong Province, Eastern China: constraints on petrogenesis and implications. *J. Asian Earth Sci.* 35 (5), 445–458. doi:10.1016/j.jseas.2009.02.008
- Liu, Y. S., Hu, Z. C., Gao, S., Günther, D., Xu, J., Gao, C. G., et al. (2008). *In situ* analysis of major and trace elements of anhydrous minerals by LA-ICP-MS without applying an internal standard. *Chem. Geol.* 257 (1–2), 34–43. doi:10.1016/j.chemgeo.2008.08.004
- Liu, Y. Z., Yang, L. Q., Wang, S. R., Liu, X. D., Wang, H., Li, D. P., et al. (2019). Origin and evolution of ore-forming fluid and gold-deposition processes at the Sanshandao gold deposit, Jiaodong peninsula, eastern China. *Minerals* 9, 189–225. doi:10.3390/min9030189
- Lowenstern, J. B., Mahood, G. A., Rivers, M. L., and Sutton, S. R. (1991). Evidence for extreme partitioning of copper into a magmatic vapor phase. *Science* 252 (5011), 1405–1409. doi:10.1126/science.252.5011.1405
- Lu, H. Z. (2011). Fluid immiscibility and fluid inclusion. *Acta Petrol. Sin.* 27 (5), 1253–1261. (in Chinese with English abstract).
- Lu, H. Z., Fan, H. R., Ni, P., Ou, G. X., Shen, K., and Zhang, W. H. (2004). *Fluid inclusions*. Beijing: Science Press, 1–450. (in Chinese).
- Ma, L., Jiang, S. Y., Dai, B. Z., Jiang, Y. H., Hou, M. L., Pu, W., et al. (2013). Multiple sources for the origin of Late Jurassic Linglong adakitic granite in the Shandong Peninsula, eastern China: zircon U-Pb geochronological, geochemical and Sr-Nd-Hf isotopic evidence. *Lithos* 162–163, 251–263. doi:10.1016/j.lithos.2013.01.009
- Ma, L., Jiang, S. Y., Hofmann, A. W., Dai, B. Z., Hou, M. L., Zhao, K. D., et al. (2014). Lithospheric and asthenospheric sources of lamprophyres in the Jiaodong Peninsula: a consequence of rapid lithospheric thinning beneath the North China Craton? *Geochim. Cosmochim. Acta* 124, 250–271. doi:10.1016/j.gca.2013.09.035
- Mao, G. Z., Hua, R. M., Long, G. M., and Lu, H. J. (2013). Rb-Sr dating of pyrite and quartz fluid inclusions and origin of ore-forming materials of the jinshan gold deposit, northeast jiangxi province, south China. *Acta Geol. Sin. Eng. Ed.* 87 (6), 1658–1667. doi:10.1111/1755-6724.12166
- Mao, J., Wang, Y., Li, H., Pirajno, F., Zhang, C., and Wang, R. (2008). The relationship of mantle-derived fluids to gold metallogenesis in the Jiaodong Peninsula: evidence from D-O-C-S isotope systematics. *Ore Geol. Rev.* 33 (3–4), 361–381. doi:10.1016/j.oregeorev.2007.01.003
- Maslennikov, V. V., Maslennikova, S. P., Large, R. R., and Danyushevsky, L. V. (2009). Study of trace element zonation in vent chimneys from the silurian yaman-kasy volcanic-hosted massive sulfide deposit (southern urals, Russia) using laser ablation-inductively coupled plasma mass spectrometry (LA-ICPMS). *Econ. Geol.* 104 (8), 1111–1141. doi:10.2113/gsecongeo.104.8.1111
- Meffre, S., Large, R. R., Steadman, J. A., Gregory, D. D., Stepanov, A. S., Kamenetsky, V. S., et al. (2016). Multi-stage enrichment processes for large gold-bearing ore deposits. *Ore Geol. Rev.* 76, 268–279. doi:10.1016/j.oregeorev.2015.09.002
- Mills, S. E., Tomkins, A. G., Weinberg, R. F., and Fan, H.-R. (2015). Anomalously silver-rich vein-hosted mineralisation in disseminated-style gold deposits, Jiaodong gold district, China. *Ore Geol. Rev.* 68, 127–141. doi:10.1016/j.oregeorev.2014.12.014
- Muntean, J. L., Cline, J. S., Simon, A. C., and Longo, A. A. (2011). Magmatic-hydrothermal origin of Nevada's Carlin-type gold deposits. *Nat. Geosci.* 4 (2), 122–127. doi:10.1038/ngeo1064
- Peterson, E. C., and Mavrogenes, J. A. (2014). Linking high-grade gold mineralization to earthquake-induced fault-valve processes in the Porgera gold deposit, Papua New Guinea. *Geology* 42 (5), 383–386. doi:10.1130/g35286.1
- Phillips, G. N., and Evans, K. A. (2004). Role of CO₂ in the formation of gold deposits. *Nature* 429 (6994), 860–863. doi:10.1038/nature02644
- Potter, J., Rankin, A. H., and Treloar, P. J. (2004). Abiogenic Fischer-Tropsch synthesis of hydrocarbons in alkaline igneous rocks, fluid inclusion, textural and isotopic evidence from the Lovozero complex, N.W. Russia. *Lithos* 75, 311–330. doi:10.1016/j.lithos.2004.03.003
- Potter, J., Rankin, A. H., Treloar, P. J., Nivin, V. A., Ting, W., and Ni, P. (1998). Preliminary study of methane inclusions in alkaline igneous rocks of the Kola igneous province, Russia: implications for the origin of methane in igneous rocks. *Eur. J. Mineral.* 10, 1167–1180. doi:10.1127/ejm/10/6/1167
- Qiu, J. S., Wang, D. Z., Luo, Q. H., and Liu, H. (2001). 40Ar–39Ar dating for volcanic rocks of Qingshan formation in Jiaolai basin, eastern Shandong province: a case study of the Fenlingshan volcanic apparatus in Wulian County. *Geol. J. China Univ.* 3, 351–355. (in Chinese with English abstract).
- Reich, M., Kesler, S. E., Utsunomiya, S., Palenik, C. S., Chryssoulis, S. L., and Ewing, R. C. (2005). Solubility of gold in arsenian pyrite. *Geochim. Cosmochim. Acta* 69 (11), 2781–2796. doi:10.1016/j.gca.2005.01.011
- Reich, M., Simon, A. C., Deditius, A., Barra, F., Chryssoulis, S., Lagas, G., et al. (2016). Trace element signature of pyrite from the los colorados iron oxide-apatite (ioa) deposit, Chile: a missing link between andean ioa and iron oxide copper-gold systems? *Econ. Geol.* 111 (3), 743–761. doi:10.2113/econgeo.111.3.743
- Ridley, J. R., and Diamond, L. W. (2000). Fluid chemistry of orogenic lode gold deposits and implications for genetic models. *Soc. Econ. Geol.* 13, 141–162. doi:10.5382/rev.13.04
- Román, N., Reich, M., Leisen, M., Morata, D., Barra, F., and Deditius, A. P. (2019). Geochemical and micro-textural fingerprints of boiling in pyrite. *Geochim. Cosmochim. Acta* 246, 60–85. doi:10.1016/j.gca.2018.11.034
- Seward, T. M. (1989). The hydrothermal chemistry of gold and its implications for ore formation: boiling and conductive cooling as examples. *Econ. Geol. Monogr.* 6, 398–404. doi:10.5382/Mono.06.31
- Simon, G., Huang, H., Penner-Hahn, J. E., Kesler, S. E., and Kao, L. S. (1999). Oxidation state of gold and arsenic in gold-bearing arsenian pyrite. *Am. Mineral.* 84 (7–8), 1071–1079. doi:10.2138/am-1999-7-809
- Song, M. C. (2015). The main achievements and key theory and methods of deep-seated prospecting in the Jiaodong gold concentration area, Shandong Province. *Geol. Bull. China* 34, 1758–1771. (in Chinese with English abstract).
- Steadman, J. A., Large, R. R., Meffre, S., Olin, P. H., Danyushevsky, L. V., Gregory, D. D., et al. (2015). Synsedimentary to early diagenetic gold in black shale-hosted pyrite nodules at the golden mile deposit, kalgoorlie, western Australia. *Econ. Geol.* 110 (5), 1157–1191. doi:10.2113/econgeo.110.5.1157

- Stefansson, A. S., and Seward, T. M. (2004). Gold(I) complexing in aqueous sulphide solutions to 500°C at 500 bar. *Geochim. Cosmochim. Acta* 68, 4121–4143. doi:10.1016/j.gca.2004.04.006
- Tardani, D., Reich, M., Deditius, A. P., Chrystosoulis, S., Sánchez-Alfaro, P., Wrage, J., et al. (2017). Copper-arsenic decoupling in an active geothermal system: a link between pyrite and fluid composition. *Geochim. Cosmochim. Acta* 204, 179–204. doi:10.1016/j.gca.2017.01.044
- Thomas, H. V., Large, R. R., Bull, S. W., Maslennikov, V., Berry, R. F., Fraser, R., et al. (2011). Pyrite and pyrrhotite textures and composition in sediments, laminated quartz veins, and reefs at Bendigo Gold Mine, Australia: insights for ore genesis. *Econ. Geol.* 106 (1), 1–31. doi:10.2113/econgeo.106.1.1
- Ueno, Y., Yamada, K., Yoshida, N., Maruyama, S., and Isozaki, Y. (2006). Evidence from fluid inclusions for microbial methanogenesis in the early Archaean era. *Nature* 446, 516–519. doi:10.1038/nature04584
- Ulrich, T., Gunther, D., and Heinrich, C. A. (2002). The evolution of a porphyry Cu–Au deposit, based on LA-ICP-MS analysis of fluid inclusions: bajo de la Alumbra. Argentina. *Econ. Geol.* 97 (8), 1743–1774. doi:10.2113/gsecongeo.96.8.1743
- Wen, B. J., Fan, H. R., Hu, F. F., Liu, X., Yang, K. F., Sun, Z. F., et al. (2016). Fluid evolution and ore genesis of the giant Sanshandao gold deposit, Jiaodong gold province, China: constrains from geology, fluid inclusions and H–O–S–He–Ar isotopic compositions. *J. Geochem. Explor.* 171, 96–112. doi:10.1016/j.gexplo.2016.01.007
- Wen, B. J., Fan, H. R., Santosh, M., Hu, F. F., Pirajno, F., and Yang, K. F. (2015). Genesis of two different types of gold mineralization in the Linglong gold field, China: constrains from geology, fluid inclusions and stable isotope. *Ore Geol. Rev.* 65, 643–658. doi:10.1016/j.oregeorev.2014.03.018
- Wu, J. J., Zeng, Q. D., Santosh, M., Fan, H. R., Bai, R., Li, X. H., et al. (2022). Deep ore-forming fluid characteristics of the Jiaodong gold province: evidence from the Qianchen gold deposit in the Jiaojia gold belt. *Ore Geol. Rev.* 145, 104911. doi:10.1016/j.oregeorev.2022.104911
- Xie, S. W., Wu, Y. B., Zhang, Z. M., Qin, Y. C., Liu, X. C., Wang, H., et al. (2012). U–Pb ages and trace elements of detrital zircons from Early Cretaceous sedimentary rocks in the Jiaolai Basin, north margin of the Sulu UHP terrane: provenances and tectonic implications. *Lithos* 154, 346–360. doi:10.1016/j.lithos.2012.08.002
- Xu, Y. W., Mao, G. Z., Liu, X. T., An, P. R., Wang, Y., and Cao, M. P. (2022). Genesis of the zhaoxian gold deposit, Jiaodong peninsula, China: insights from *in-situ* pyrite geochemistry and S–He–Ar isotopes, and zircon U–Pb geochronology. *Front. Earth Sci.* 10, 886975. doi:10.3389/feart.2022.886975
- Yang, K. F., Fan, H. R., Santosh, M., Hu, F. F., Wilde, S. A., Lan, T. G., et al. (2012). Reactivation of the Archean lower crust: implications for zircon geochronology, elemental and Sr–Nd–Hf isotopic geochemistry of late Mesozoic granitoids from northwestern Jiaodong terrane, the North China craton. *Lithos* 146–147, 112–127. doi:10.1016/j.lithos.2012.04.035
- Yang, K. F., Jiang, P., Fan, H. R., Zuo, Y. B., and Yang, Y. H. (2018). Tectonic transition from a compressional to extensional metallogenic environment at ~120 Ma revealed in the Hushan gold deposit, Jiaodong, North China Craton. *J. Asian Earth Sci.* 160, 408–425. doi:10.1016/j.jseas.2017.08.014
- Yang, L. Q., Deng, J., and Wang, Z. L. (2014). Mesozoic gold metallogenic system in Jiaodong. *Acta Petrol. Sin.* 30 (9), 2447–2467. (in Chinese with English abstract).
- Yang, L. Q., Deng, J., Wang, Z. L., Guo, L. N., Li, R. H., Groves, D. I., et al. (2016). Relationships between gold and pyrite at the Xincheng gold deposit, Jiaodong Peninsula, China: implications for gold source and deposition in a brittle epizonal environment. *Econ. Geol.* 111, 105–126. doi:10.2113/econgeo.111.1.105
- Yang, L.-Q., Guo, L.-N., Wang, Z.-L., Zhao, R.-X., Song, M.-C., and Zheng, X.-L. (2017). Timing and mechanism of gold mineralization at the Wangershans gold deposit, Jiaodong Peninsula, eastern China. *Ore Geol. Rev.* 88, 491–510. doi:10.1016/j.oregeorev.2016.06.027
- Yang, M. Z. (1998). *The Geochemistry of wallrock alteration zone of gold deposits — as exemplified by Jiaodong gold deposits*, 109–112. (in Chinese).
- Yang, S. W. (1986). A discussion on the Jiaodong Group strata, the source-bed of gold and the strata-bound features of gold ore deposits in northwest part of Jiaodong peninsula. *Contrib. Geol. Min. Res.* 1 (2), 1–12. (in Chinese with English abstract). doi:10.6053/j.issn.1001-1412.1986.2.001
- Zhai, M. G., Fan, H. R., Yang, J. H., and Miao, L. C. (2004). Large-scale cluster of gold deposits in east Shandong: anorogenic metallogenesis. *Earth-Sci. Front.* 11 (1), 85–98. (in Chinese with English abstract). doi:10.1016/S0960-0779(03)00420-X
- Zhai, M. G., and Santosh, M. (2013). Metallogeny of the North China Craton: link with secular changes in the evolving earth. *Gondwana Res.* 24 (1), 275–297. doi:10.1016/j.gr.2013.02.007
- Zhang, W., Hu, Z., and Liu, Y. (2020). Iso-Compass: new freeware software for isotopic data reduction of LA-MC-ICP-MS. *J. Anal. At. Spectrom.* 35 (6), 1087–1096. doi:10.1039/D0JA00084A
- Zhang, Z. M., Zeng, Q. D., Wang, Y. B., Guo, Y. P., Yu, B., Wang, R. L., et al. (2023). Metallogenic age and fluid evolution of the Kangshan Au-polymetallic deposit in the southern margin of the North China Craton: constraints from monazite U–Pb age, and *in-situ* trace elements and S isotopes of pyrite. *Acta Petrol. Sin.* 39 (3), 865–885. (in Chinese with English abstract). doi:10.18654/1000-0569/2023.03.14
- Zhou, J. B., Wilde, S. A., Zhao, G. C., Zhang, X. Z., Zheng, C. Q., Jin, W., et al. (2008). SHRIMP U–Pb zircon dating of the wulian complex: defining the boundary between the North and south China cratons in the Sulu orogenic belt, China. *Precamb. Res.* 162 (3–4), 559–576. doi:10.1016/j.precamres.2007.10.008
- Zhou, T. H., and Lü, G. X. (2000). Tectonics, granitoids and mesozoic gold deposits in east Shandong China. *Ore Geol. Rev.* 16, 71–90. doi:10.1016/S0169-1368(99)00023-2
- Zhu, D. C., Zhang, W., Wang, Y. P., Tian, J. X., Liu, H. D., Hou, J. H., et al. (2018). Characteristics of ore bodies and prospecting potential of Zhaoxian gold deposit in Laizhou city of Shandong province. *Shandong Land Resour.* 34 (9), 14–19. (in Chinese with English abstract).
- Zhu, R. X., Fan, H. R., Li, J. W., Meng, Q. R., Li, S. R., and Zeng, Q. D. (2015). Decratonic gold deposits. *Sci. China Earth Sci.* 58 (9), 1523–1537. doi:10.1007/s11430-015-5139-x
- Zong, K. Q., Klemd, R., Yuan, Y., He, Z. Y., Guo, J. L., Shi, X. L., et al. (2017). The assembly of Rodinia: the correlation of early Neoproterozoic (ca. 900 Ma) high-grade metamorphism and continental arc formation in the southern Beishan Orogen, southern Central Asian Orogenic Belt (CAOB). *Precamb. Res.* 290, 32–48. doi:10.1016/j.precamres.2016.12.010
- Zou, Y., Zhai, M. G., Santosh, M., Zhou, L. G., Zhao, L., Lu, J. S., et al. (2017). High-pressure pelitic granulites from the Jiao-Liao-Ji Belt, North China Craton: a complete P–T path and its tectonic implications. *J. Asian Earth Sci.* 134, 103–121. doi:10.1016/j.jseas.2016.10.015